


RESEARCH ARTICLE

Relationships between summertime surface albedo and melt pond fraction in the central Arctic Ocean: The aggregate scale of albedo obtained on the MOSAiC floe

Radiance Calmer^{1,2,*} , Gijs de Boer^{1,2,3}, Jonathan Hamilton^{1,3}, Dale Lawrence⁴, Melinda A. Webster^{5,6}, Nicholas Wright⁷, Matthew D. Shupe^{1,3}, Christopher J. Cox³, and John J. Cassano^{1,8,9}

As part of the Multidisciplinary drifting Observatory for the Study of Arctic Climate (MOSAIC), the HELiX uncrewed aircraft system (UAS) was deployed over the sea ice in the central Arctic Ocean during summer 2020. Albedo measurements were obtained with stabilized pyranometers, and melt pond fraction was calculated from orthomosaic imagery from a surface-imaging multispectral camera. This study analyzed HELiX flight data to provide insights on the temporal and spatial evolution of albedo and melt pond fraction of the MOSAiC floe during the melt season as it drifted south through Fram Strait. The surface albedo distributions showed peak values changing from high albedo (0.55–0.6) to lower values (0.3) as the season advanced. Inspired by methods developed for satellite data, an algorithm was established to retrieve melt pond fraction from the orthomosaic images. We demonstrate that the near-surface observations of melt pond fraction were highly dependent on sample area, offering insight into the influence of subgrid scale features and spatial heterogeneity in satellite observations. Vertical observations conducted with the HELiX were used to quantify the influence of melt pond scales on observed surface albedo as a function of sensor footprint. These scaling results were used to link surface-based measurements collected during MOSAiC to broader-scale satellite data to investigate the influence of surface features on observed albedo. Albedo values blend underlying features within the sensor footprint, as determined by the melt pond size and concentration. This study framed the downscaling (upscaling) problem related to the airborne (surface) observations of surface albedo across a variety of spatial scales.

Keywords: Albedo, Melt pond fraction, Central Arctic, Sea ice, Uncrewed aircraft system, Multispectral imagery

¹Cooperative Institute for Research in Environmental Sciences, University of Colorado, Boulder, CO, USA

²Integrated Remote and In Situ Sensing (IRISS), University of Colorado, Boulder, CO, USA

³NOAA Physical Sciences Laboratory, Boulder, CO, USA

⁴Smead Aerospace Engineering Sciences, University of Colorado, Boulder, CO, USA

⁵Geophysical Institute of the University of Alaska Fairbanks, AK, USA

⁶Polar Science Center, University of Washington, Seattle, WA, USA

⁷U.S. Army Cold Regions Research and Engineering Laboratories, Hanover, NH, USA

⁸National Snow and Ice Data Center, University of Colorado, Boulder, CO, USA

⁹Department of Atmospheric and Oceanic Sciences, University of Colorado, Boulder, CO, USA

* Corresponding author:

Email: radiance.calmer@colorado.edu

1. Introduction

The last decade has seen record minimum Arctic sea ice coverage and thickness. Climate models predict that summers may be completely free of ice prior to 2050 (Intergovernmental Panel on Climate Change, 2021). This decline of sea ice has been documented using satellite-based sensors (e.g., Comiso et al., 2008; Meier et al., 2022), which have provided observations of thinner ice cover (Rothrock et al., 1999; Perovich et al., 2003) and a general decrease in multiyear ice (MYI; Maslanik et al., 2011). This decline in sea ice has many repercussions locally and globally, including significant impacts on the Arctic's freshwater system and surface energy budget (Serreze et al., 2007), alteration of marine primary production with impacts on ecosystems (Meredith et al., 2019), and perturbations to midlatitude circulation and precipitation patterns (Vihma, 2014).

When investigating the major drivers of Arctic change, the ice albedo feedback is described as one of the main processes spurring the melt of sea ice (Hall, 2004; Screen and Simmonds, 2010; Thackeray et al., 2019; Wunderling et al., 2020). The ice-ocean albedo feedback is a positive feedback loop, where a reduction in highly reflective snow and ice area results in an increase in the areal fraction of dark ocean surface, thereby reducing the overall albedo of the Arctic regions. This change results in increased absorption of solar energy into the upper ocean, increasing ocean temperatures and inhibiting sea ice growth (Kashiwase et al., 2017). As the Arctic climate changes, the melt and freeze onsets shift in time. Based on passive microwave satellite measurements (Stroeve et al., 2014), the melt season is observed to lengthen 5 days per decade. Melt onset impacts the pond formation and the sea ice summer energy balance as more solar energy is absorbed and stored in the ice-ocean system (Perovich et al., 2020).

Melt ponds play an important role in governing the albedo of summertime Arctic sea ice. It is therefore critical to understand and simulate the development, evolution, and overall influence of these features. Studies of melt pond coverage have been conducted using ground-based (Perovich et al., 2002a; Polashenski et al., 2012), airborne (Perovich et al., 2002b), and satellite observations (Fetterer and Untersteiner, 1998; Tschudi et al., 2007; Kwok, 2013; Webster et al., 2015; Pohl et al., 2020). Numerous flights to study ice properties in the Arctic were conducted during Operation IceBridge (MacGregor et al., 2021), providing a large open-access data set, supporting detailed studies of melt pond coverage (Buckley et al., 2020; Wright et al., 2020). Early on, a linear relationship was determined between melt pond fraction and albedo in the Canadian Arctic using pyranometers suspended from a helicopter and photographs of the surface (Langleben, 1971), but this slope was highly dependent on the study area. A radiative transfer model has been applied to Arctic sea ice and fast ice to evaluate the impact of surface features on the partitioning of solar radiation. The dependence of solar transmittance was identified based on the thickness of snow and sea ice and the amount of particle matter and biomass present in the ice (Zhu et al., 2021). The large amount of solar energy absorbed by melt ponds rather than the underlying sea ice was also established by the radiative transfer model for thin ice (Lu et al., 2016; Lu et al., 2018), highlighting the importance of pond depths in the study of surface albedo. Nonetheless, because of the lack of in situ observations, particularly of underlying ice, and the thinning of the Arctic sea ice over the past decades, comparisons between model results and observations were precarious. Connecting atmospheric variabilities and surface albedo, snow albedo under clear skies generally increases with solar zenith angle because photons are more likely to be scattered out when entering the surface at an angle (Warren, 1982). However, because of the dominant effect of spectral shifts toward higher frequencies under cloud cover, diffuse albedo over snow is still typically higher than clear-sky albedo even when the solar zenith angle is larger than the effective diffuse incidence angle (Warren, 1982). Stapf et al. (2020)

investigated cloud radiative forcing in the Arctic Marginal Ice Zone as a function of cloud liquid water path and solar zenith angles for different surface types. Broadband surface albedo over snow and sea ice increased for cloudy skies compared to clear skies. This result agreed with Grenfell and Perovich (2008) study, which also included melt ponds as a surface type. Wavelength-integrated albedo varied by as much as 10% between clear and cloudy skies, with higher variations on snow and bare ice. Nonetheless, Stapf et al. (2020) also emphasized the role of variability in sea ice concentration for the observed fluctuation in surface albedo and the importance of obtaining albedo on the effective areally averaged surface. Field experiments like those associated with the Surface Heat Budget of the Arctic (Uttal et al., 2002) and Multidisciplinary drifting Observatory for the Study of the Arctic Climate (MOSAiC; Nicolaus et al., 2022; Shupe et al., 2022) expeditions have provided detailed perspectives on the seasonal evolution of the Arctic surface, linking albedo, surface state, and the surface energy budget over the seasonal cycle (Perovich et al., 2002a). During the spring and summer melt season, several critical features have been observed and documented, including information on the influence of the sea ice surface scattering layer on bare ice albedo (Smith et al., 2022) and the highly variable albedo of a ponded ice surface (Light et al., 2022). Melt pond evolution, depth and aerial fraction, was also intensely reported during MOSAiC using in situ surveys (Webster et al., 2022). Melt pond depth was studied using novel methods (Linhardt et al., 2021). These surface features and the processes that govern their existence make the summer sea ice challenging to understand and model. Recently, the MOSAiC expedition offered a different opportunity to study melt-pond-relevant processes through the analyses of measurements collected on and around a single ice floe over the course of an entire annual cycle. The collaborative work of scientists from different fields (atmosphere, sea ice, ocean, biology, and biochemistry) created a multidisciplinary approach, supporting the deployment of complementary instruments to investigate climate processes from different perspectives.

In addition to space-, aircraft-, and surface-based perspectives, recent years have seen the deployment of a small number of uncrewed aircraft systems (UAS) over Arctic sea ice. These efforts include flights conducted using the Aerosonde UAS, which flew over the Arctic Ocean from coastal Alaska to collect the images of sea ice and estimate melt pond fraction (Inoue et al., 2007). Aerosonde images were also used to validate the estimate of melt pond coverage using the satellite-based Moderate Resolution Imaging Spectroradiometer retrievals (Tschudi et al., 2007). More recently, a DJI Phantom 4 was deployed from the Chinese R/V Xuelong icebreaker over an ice floe in the Canadian Basin (Wang et al., 2018), and the University of Alaska Sea Hunter UAS was operated in near-coastal regions along the Alaskan and Canadian coastlines (de Boer et al., 2019b). However, these UAS activities only represent very short-term focused efforts over limited time windows to study melt pond evolution and surface roughness. Additionally, these efforts generally sampled over a variety of

flight paths, thereby making it challenging to track the evolution of sea ice and melt pond conditions over an individual ice floe.

As a part of the recent MOSAiC campaign, the University of Colorado Boulder and NOAA Physical Sciences Laboratory deployed 2 types of UAS over the summertime sea ice in the central Arctic. One of these systems was a hexacopter platform named HELiX, dedicated to collecting information on the evolution of surface properties during the melt season, including surface albedo and melt pond fraction. The HELiX was deployed repeatedly over a common ice floe from late June to beginning of August when the floe transitioned from the pack ice, to the marginal ice zone, and finally to its demise in the North Atlantic (Shupe et al., 2022). During this time, the HELiX provided high-resolution measurements of the surface, bridging a range of spatial scales from in situ point measurements to satellite footprints. As the HELiX was operated at low altitudes in clear, cloudy, and foggy skies, it did not suffer from the challenges associated with satellite-based observing in the cloud-filled Arctic region (Tschudi et al., 2007; Kwok, 2013) or need to account for aerosol attenuation of light between the surface and sensor system (Jakel et al., 2013). Similar instrumentation, pyranometers and camera, has already been flown on board of a fixed-wing UAS above the Greenland ice sheet and over northern Alaska as part of the Evaluation or Routine Atmospheric Sounding Measurements using Unmanned Systems campaign (de Boer et al., 2019a). However, the HELiX data set represents, to our knowledge, the first extended UAS-based observation of surface albedo over the central Arctic.

This manuscript introduces measurements from the HELiX during the sea ice melting period, providing broadband albedo and melt pond fraction over first year and multiyear portions of the MOSAiC ice floe. Together with complementary data sets from surface- and satellite-based sensors, the HELiX observations are used to provide a detailed perspective on the scaling of surface features and surface albedo of the MOSAiC floe. The first section presents information about the HELiX flights and describes the methods used to calculate albedo and melt pond fraction. This is followed by an overview of the results derived from all of the HELiX flights, including a description of the surface changes over time and specific events that occurred during the summer measurement period. The last section focuses on a case study to investigate the impact of the measurement altitude and the melt pond dimensions on albedo results. Then, using a satellite image, the study is extended from the HELiX flight to other locations on the MOSAiC ice floe. A summary of the results and discussions concludes the manuscript.

2. Methods

This study utilizes data collected by the HELiX UAS. The HELiX is equipped with stabilizing gimbals both above and below the platform to maintain precise nadir and zenith orientation of customized Kipp and Zonen PR1 pyranometers. These sensors cover a spectral range of 310–2,700 nm, with the 2 sensors together providing the up- and downwelling broadband shortwave irradiance, as

well as net irradiance, when considering the difference between the two. In addition to the PR1s, the lower gimbal carried a RedEdge-MX multispectral camera. This camera is configured to capture images with 80% overlap in 5 spectral channels, including blue (475 nm), green (560 nm), red (668 nm), red (717 nm), and near-infrared (842 nm). The individual images of the surface are assembled in postprocessing to create orthomosaic images and reflectance maps. The resolution of the images varies between 0.006 and 0.193 m/pixel depending on the HELiX flight altitude. Orthomosaic image areas cover rectangles from 150 m × 110 m to 370 m × 335 m. More details on the instrumentation can be found in de Boer et al. (2022), including a description of the quality control processes applied to the HELiX data. Methods presented hereafter use the quality-controlled and synchronized data set from the onboard data logger (Calmer et al., 2021) and from the multispectral camera (Hamilton et al., 2021).

During summer 2020 of the MOSAiC expedition, the HELiX UAS flew 34 flights (see Supplemental Material Table S1). These flights occurred between June 26, 2020, and August 6, 2020, and included a combination of 3 different flight patterns. Flight patterns consisted of vertical profiles up to 380 m, horizontal grid pattern flights covering around 200 m × 300 m, and extended hovers above defined surface areas. Flights occurred mainly at 2 locations on the MOSAiC floe; one site over first year ice (FYI) and an MYI site located near the MOSAiC “Met City.” The majority of the flights took place under low clouds with diffuse light conditions. Focusing on profile and grid patterns, for 2 flights (FL14 and FL20), a cloud ceiling at around 1,000 m was present. Three flights (FL04, FL19, and FL34) took place under clear sky in direct sunlight. In 2 flights (FL14 and FL19), downwelling shortwave irradiance was corrected for small angular offsets in the gimbal based on comparison with the pyranometer deployed ground-based on flux station located at the surface beneath the flight pattern (de Boer et al., 2022). To ensure that variability in measured albedo during the grid flights was directly linked to surface features and not atmospheric conditions due to low-level clouds or fog, downwelling shortwave irradiance from FL27 on July 27, 2020, and from the Atmospheric Surface Flux Station 50 (ASFS50, Cox et al., 2021) are compared in Figure S1. Measurements from the UAS are similar to those of the ASFS50, indicating that the albedo observations from the grid flights in diffuse conditions were essentially independent of atmospheric variability.

The SkySat satellite image in **Figure 1** (Wright et al., 2021) shows the MOSAiC floe on July 7, 2020, and captures the areas where the HELiX flew. Features on the ice floe, such as melt ponds, can be used to identify the HELiX flight locations within the broader satellite image and provide perspectives on the location of these flights relative to MOSAiC’s support vessel, R/V *Polarstern*, and other expedition assets. The satellite scene additionally provides an overview of the composition of the ice surface above which the HELiX operated. In addition to HELiX measurements, there were several other sensors measuring radiation and albedo in the vicinity. For example, manual

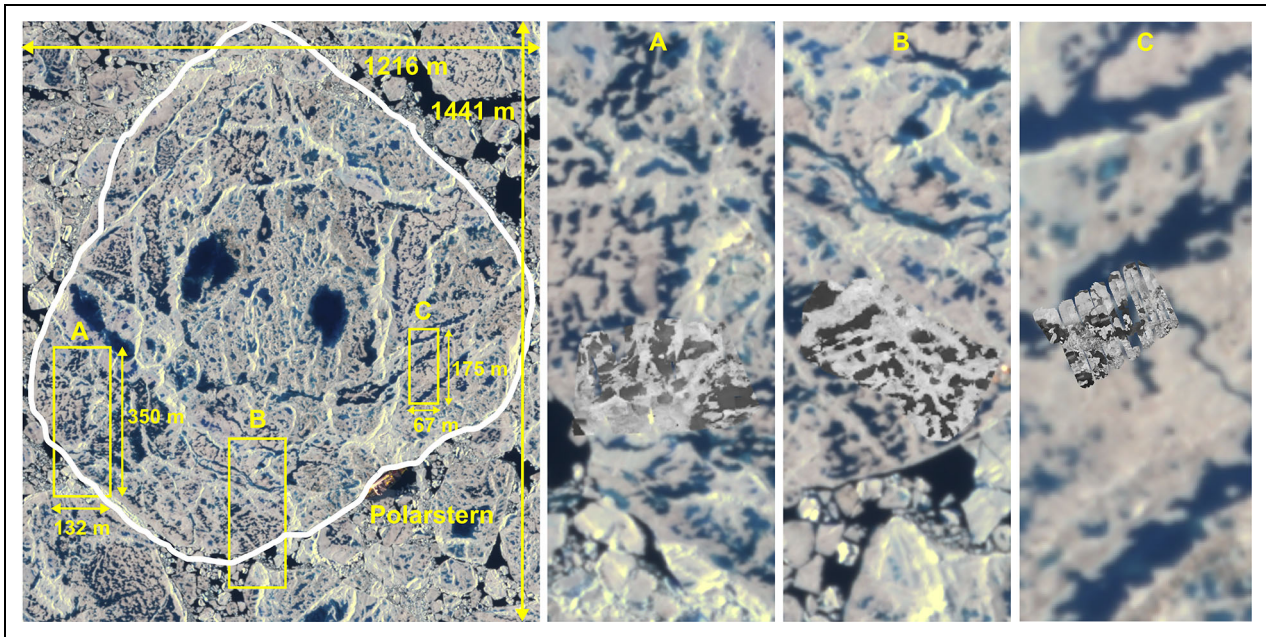


Figure 1. SkySat satellite multispectral image for the MOSAiC floe. Imagery © 2022 Planet Labs Inc. The Polarstern is at the bottom right of the image (resolution 50 cm/pix). Yellow rectangles correspond to identified areas: (A) First year ice area, (B) remotely operated vehicle area, and (C) Met City area. Orthomosaics from the HELiX flights (grayscale) are overlaid on the zoom areas of the satellite image. Dates of the images: satellite on July 7, 2020, HELiX orthomosaic (A) July 6, 2020, HELiX orthomosaic, (B) July 10, 2020, HELiX orthomosaic, and (C) July 17, 2020. MOSAiC = Multidisciplinary drifting Observatory for the Study of Arctic Climate.

sampling of surface-based albedo along transect lines was executed to provide regular observations of albedo across a variety of surfaces. These albedo lines were conducted on the FYI (**Figure 1** rectangle A), and an initial comparison of albedos measured along these albedo lines and those obtained from the HELiX UAS is provided in Nicolaus et al. (2022). Additional albedo and transmittance measurements were collected above the area where an underwater remotely operated vehicle (Rabe et al., 2022) conducted measurements (**Figure 1** rectangle B), as well as over the MYI (**Figure 1** rectangle C) area around Met City (Shupe et al., 2022). These locations were selected for intercomparison studies but also for logistical reasons.

To provide perspective on the connection between HELiX-measured albedo and surface type, a feature identification method has been adapted using techniques from Webster et al. (2015). In this method, the different channels of the multispectral camera imagery are used to segregate between different surface types, including snow/bare ice, melt pond, and ocean. For a given flight, a limited number of samples (approximate area 7.5 m²) known to be of a certain surface type are visually selected. **Figure 2a** shows the example orthomosaic from FL05 on July 1, 2020, in the multispectral camera blue channel (475 nm) with red rectangles identifying melt pond samples, yellow rectangles identifying ice samples, and blue rectangles identifying open ocean. **Figure 2b** shows the mean and standard deviation of pixel intensity for each of these sample areas in each image channel (blue, green, red, and near-infrared). Pixel intensities in each channel vary from 0 to 255. Over the ocean, pixels show only

a narrow variation of intensity across the 5 channels while melt ponds vary from brighter intensities in the blue channel to darker values in the near-infrared channel. Depending on the melting state of the ice, some overlap of pixel intensities is visible between ponds and snow/bare ice in certain channels. However, there are 2 clear gaps in the spectral data that provide unambiguous distinctions for this set of samples: the blue channel is used to define a threshold between open ocean and melt pond (**Figure 2b** dashed line) and the near-infrared channel provides a threshold value between pond and ice (**Figure 2b** solid line). These 2 thresholds are calculated for each flight to account for changes resulting from solar intensity and reflectance, and results are color-coded as in **Figure 2c**, where open ocean, melt pond, and snow/bare ice pixels are, respectively, purple, orange, and yellow.

For most flights, this classification sufficiently distinguishes between these 3 feature types; however, some cases require further processing to overcome ambiguous or incorrect classification. For example, ridge shadows can be misclassified as pond due to their darker color. Consequently, it is difficult to differentiate shadows from ponds using the RedEdgeMX imagery. Manual inspection of many images suggests that the contribution of ridge shadows to the total melt pond area is minimal, such that this potential contribution is neglected in this study. In Webster et al. (2015), the ridge shadows were found to make up less than approximately 0.5% of satellite scenes (15 km × 15 km to 30 km × 30 km) in March and April, when one would expect shadows to be most widespread due to low-angle sunlight. That result is dependent on both time of

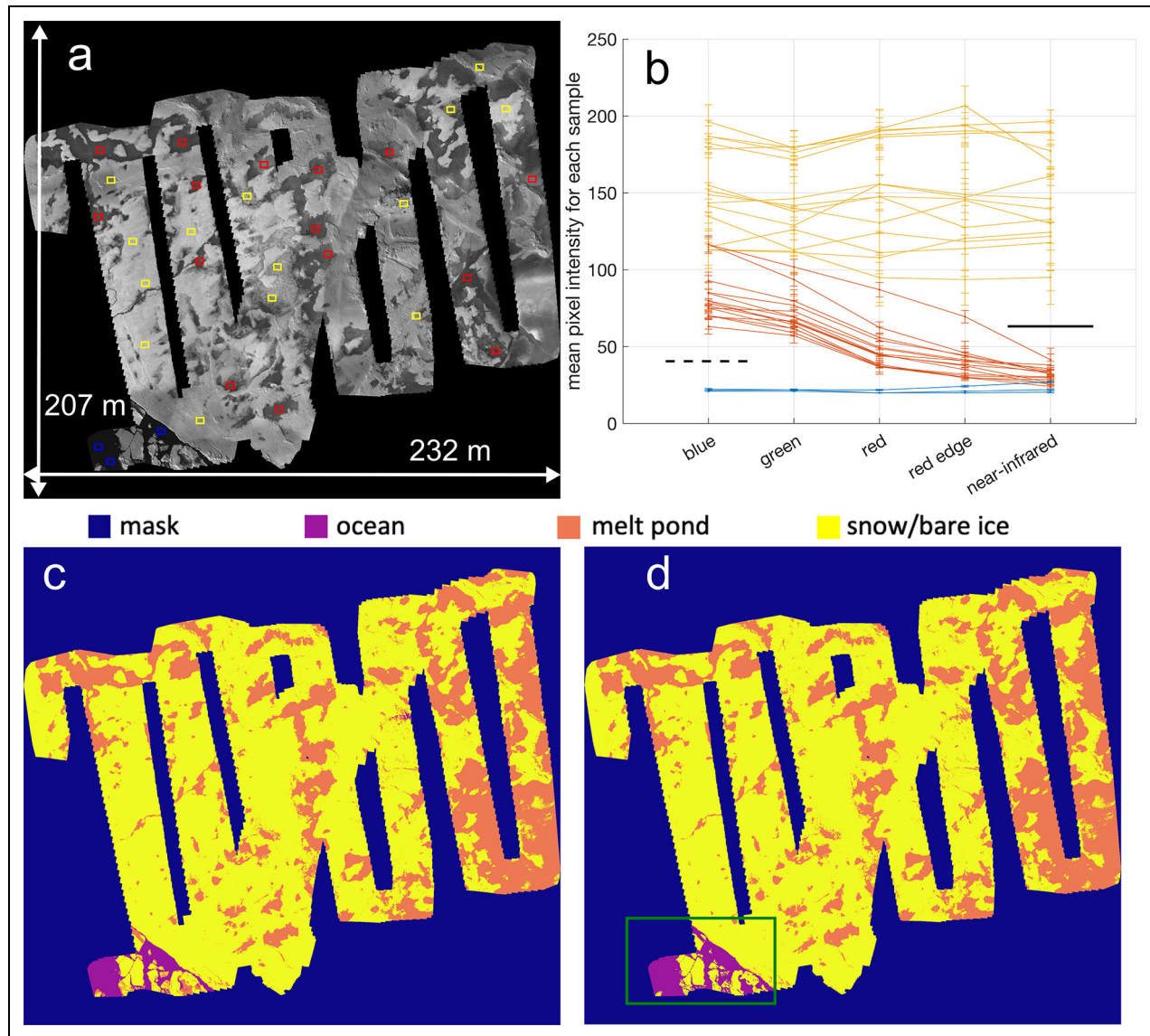


Figure 2. Identification of surface features from the HELiX orthomosaic imagery. (a) HELiX orthomosaic from the RedEdge “blue” channel on July 1, 2020; yellow rectangles are selected samples over snow/bare ice, red rectangles are melt pond samples, and blue rectangles are ocean samples. (b) Corresponding mean pixel intensity and standard deviation (error bars) for each of these rectangle samples in each color channel, where yellow lines correspond to snow/bare ice samples, red lines are pond samples, and blue lines are ocean samples. The dashed horizontal line in the blue channel marks a clearly defined threshold between ocean and pond pixel intensity, and the solid horizontal line marks a clearly defined threshold in the near-infrared channel to differentiate between pond and ice pixel intensity. (c) Results of the classification using these thresholds for the orthomosaic features. (d) The same as (c) with submerged pieces of ice classified as ocean (purple) instead of melt pond (orange) in the green rectangle.

year and ice conditions. Still, that result, combined with the fact that the HELiX flights took place in midsummer in more direct light and in mostly diffuse-light conditions (cloudy skies), likely makes it a safe assumption that ridge shadows had a negligible impact on the classification results in this study. Ice-based instruments or their shadows can also be misclassified as ponds. Nonetheless, human activities are not systematically present in the images, and their influence is calculated to impact the observed melt pond fraction by $<0.2\%$ based on an identified box present in the orthomosaic of FL04. Therefore, we also neglect the influence of ice-based instruments on

feature classification. Another issue not addressed easily with the threshold method described above is the identification of broken ice in the ocean along the floe edge. The submerged part of this broken ice has a similar spectral signature to melt ponds, although the water overlaying this ice is that from the open ocean. Open ocean is sampled in 7 of the flights, with the area varying from 3% to 40% of the total image area due to ice dynamics surrounding the floe. Therefore, an additional mask is created over the ocean, and within these selected areas, pixels identified as pond are then adjusted to open ocean value (see **Figure 2d**). This step removes submerged ice in open

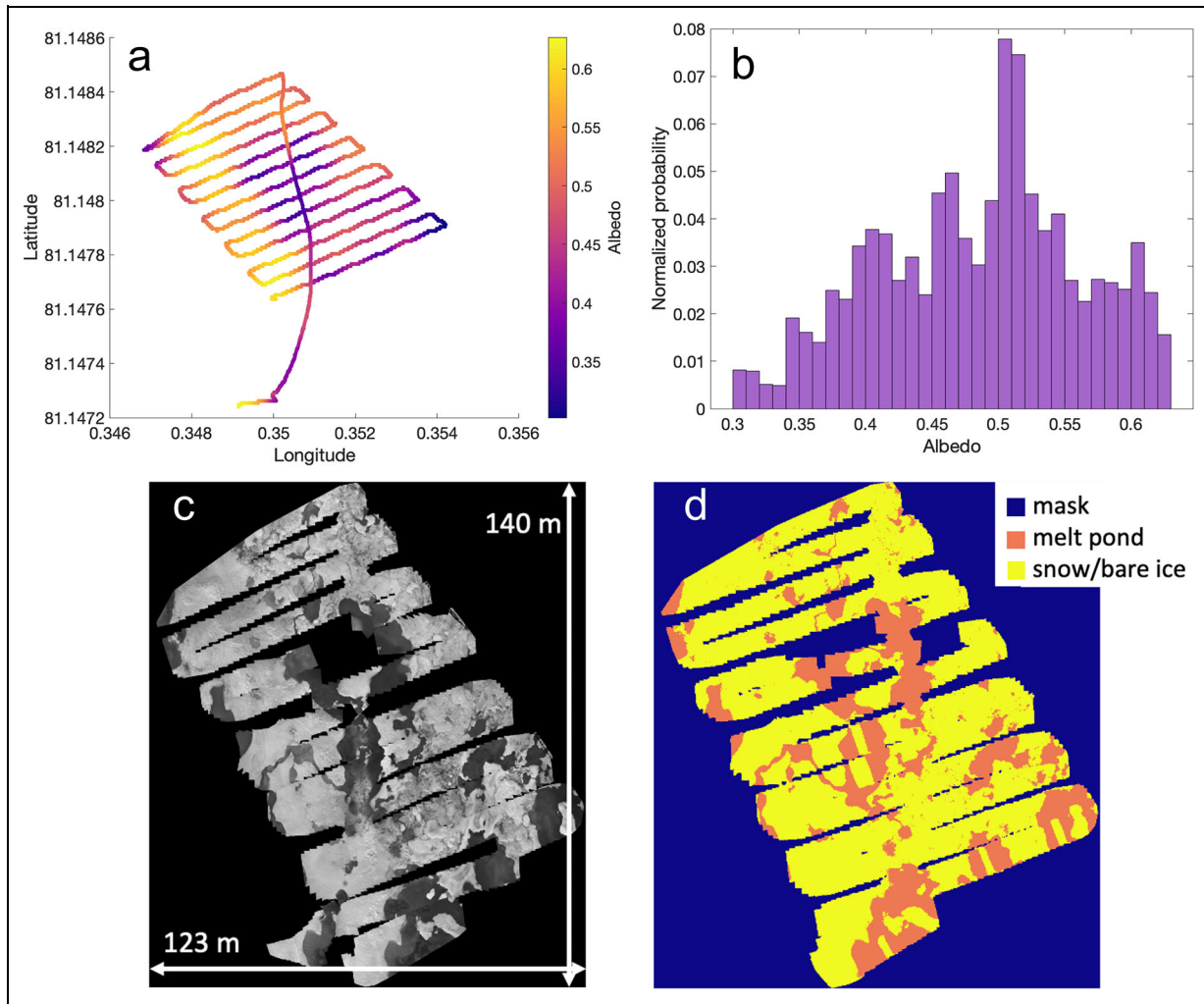


Figure 3. HELiX flight FL14 on July 17, 2020. (a) HELiX flight pattern color-coded with measured albedo, (b) corresponding normalized histogram of albedo, (c) associated orthomosaic from the multispectral camera, and (d) results of the feature classification of the orthomosaic.

ocean areas from the calculated melt pond area. With these corrections to the classification scheme, melt pond fraction can be calculated as:

$$\frac{\text{melt pond area}}{\text{sea ice area}} \times 100,$$

with sea ice area = melt pond area + snow area + bare ice area.

For the example of FL05 provided in **Figure 2**, snow/bare ice and melt pond areas represent 23,649 m² and melt pond area is 6,391 m², resulting in a melt pond fraction of 27%. Following the definition of the error types in surface identification introduced by Wright and Polashenski (2018), the present study shows external errors due to the image resolution as a pixel can represent multiple surface types within its boundaries. The internal error occurs for features that are in a transitional state, for example, dark snow transitioning to a melt pond. This type of error is too difficult to identify for a human observer. In both cases, the assumption is made that the pixel color will be equal or close to the threshold defined in the study

of each orthomosaic (**Figure 2b**). To account for uncertainty in surface classification coming from the image resolution or the transitional state, the thresholds are moved by ± 2 in the grayscale intensity. Results provide 0.1%–1.8% of the pixel images are potentially misclassified as no clear answer can be obtained for these pixels. As expected, these pixels are located at the edge of the melt ponds or the transition between the ocean and submerged ice. Uncertainty on surface classification is then $0.4\% \pm 0.4\%$.

Figure 3 provides an example of HELiX measurements during a horizontal grid flight (FL14), applying the methods described above. The flight pattern is color-coded with albedo as measured by the pyranometers in **Figure 3a**, and the corresponding distribution of albedos is shown in **Figure 3b**. When looking at the orthomosaic image (**Figure 3c**), low albedo (<0.4) areas are associated with melt ponds, whereas reflective surfaces (albedo > 0.55) are identified visually on the image as bare ice. This assessment is corroborated using the classification techniques (**Figure 3d**). It should be noted that the pyranometer measurements likely underestimate the full breadth of the albedo distribution, because they make cosine-weighted

hemispheric measurements, which means that at the altitude of the HELiX UAS (approximately 10 m in this case), there is some averaging of the albedo from neighboring ice and pond surfaces in the reflected radiative flux of observations.

3. Results

3.1. Albedo

Grid flights are selected from the 3 different flight patterns to investigate the evolution of albedo as a function of time and altitude. **Figure 4a** associates flight numbers with the corresponding date for all grid-pattern flights. Markers are color-coded by albedo in **Figure 4b**, with the mean value of albedo displayed at the geographical location depending on the drift of the MOSAiC ice floe. The mean value of albedo is calculated from observations collected at the grid flight altitude only, disregarding take-off and landing phases to avoid biases. A general decrease of mean albedo can be observed as the MOSAiC floe drifts from the northeast to the southwest. The most significant exception to this pattern is the last flight (FL34 on

August 6), which features a mean albedo around 0.45 (orange rectangle at the bottom left of **Figure 4b**). This outlier can be explained as the MOSAiC floe had already been dislocated and the flight took place in the marginal ice zone over a different floe, which presented a different repartition of features (bare ice/melt pond/ocean). Diffuse solar fluxes were measured by Delta-T SPN1 pyranometers at Met City and 2 locations on board the Polarsten (Shupe et al., 2022). **Figure 4c** provides the diffuse fraction obtained by diffuse solar flux divided by downwelling shortwave radiative flux. Values displayed in **Figure 4c** are averaged for the 3 locations and over the flight time and shown as a function of the associated solar zenith angle for the HELiX grid flight time. Based on the previous studies, a lower surface albedo value might be expected for flights in clear sky conditions with a diffuse fraction lower than 0.4. However, comparing **Figure 4b** and **c**, the impact of time as the melt season progresses with larger surface variability is predominant compared to the impact of clear sky/

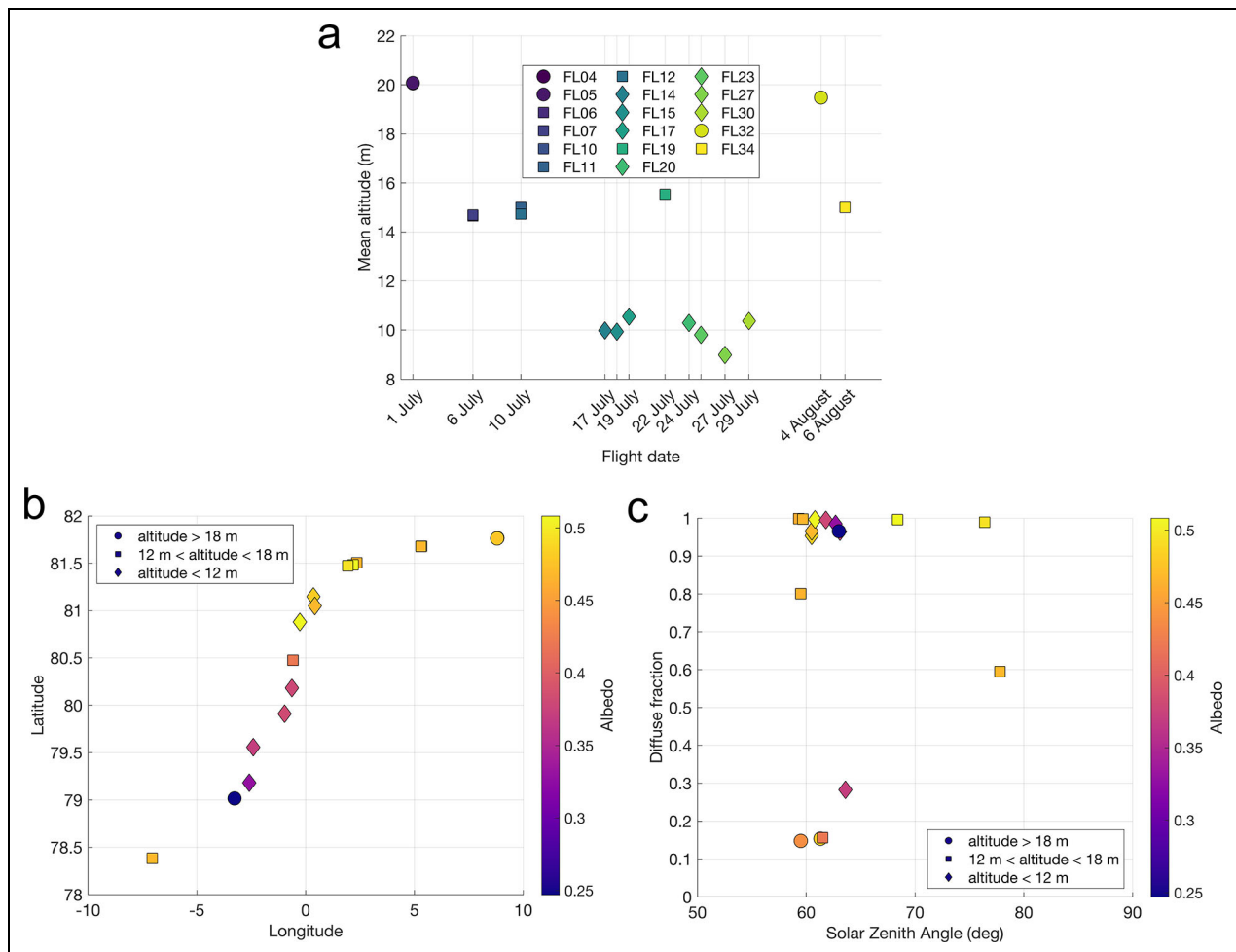


Figure 4. HELiX grid flights. (a) HELiX grid flight dates and altitudes color-coded by time, (b) HELiX grid flight geographical locations color-coded by albedo, and (c) solar zenith angles as a function of diffuse fraction for each HELiX grid flight color-coded by albedo. The shapes of markers in (a), (b), and (c) represent the grid flight altitude, with circles for mean flight altitudes higher than 18 m, rectangles for mean flight altitudes between 12 and 18 m, and diamonds for flight mean altitudes lower than 12 m. Note that markers for FL04 and FL05 are on top of each other as these flights took place during the same afternoon.

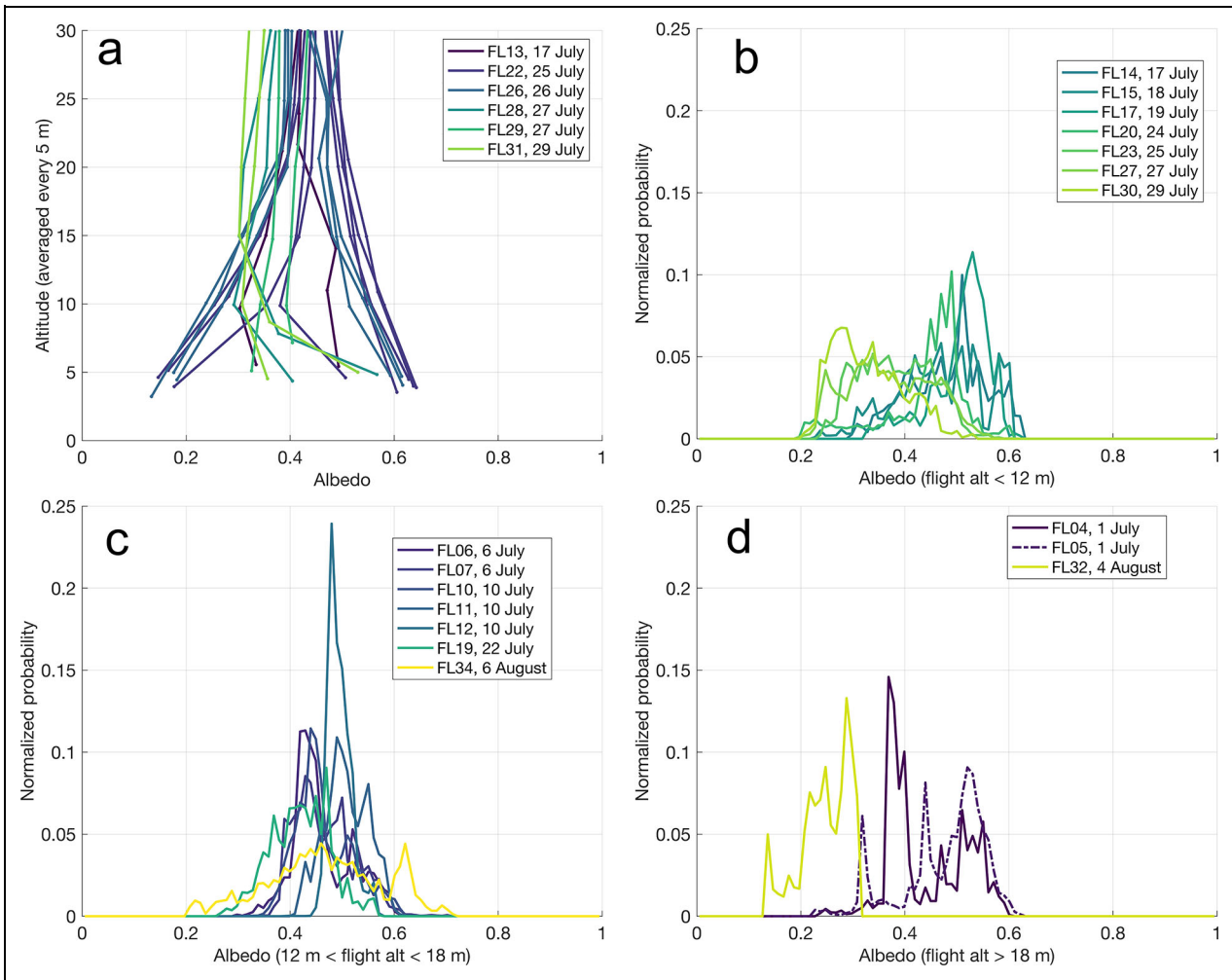


Figure 5. HELiX albedo from the vertical profiles and distributions from the horizontal grid flights. (a) HELiX vertical profile flights with albedo averaged for each 5-m bin in altitude and displayed only between the surface and 30 m. (b) Albedo distributions for horizontal grid flights below 12 m, (c) albedo distributions for horizontal grid flights between 12 and 18 m, and (d) albedo distributions for horizontal grid flights higher than 18 m. The flights are color-coded by date (see **Figure 4a**), dark blue for the beginning and yellow for the end of the campaign.

cloudy conditions on surface albedo measured by the HELiX.

While time of year and latitudinal location are important factors to consider when interpreting the albedo evolution of sea ice, the altitude at which an albedo measurement is made is also a key consideration for appropriately interpreting albedo data. This is particularly important when comparing albedo time series between different measurement techniques (e.g., surface-based, satellite-derived). To complement observations from the horizontal gridded flights, vertical profile flights are introduced in **Figure 5a**. **Figure 5a** shows albedo measured between the surface and 30 m, with albedo values averaged using 5-m vertical bins. Each color represents an independent flight profile color-coded by time, with profiles starting over different surface types. Depending on the type of surface feature that the HELiX was over at the start of its profile, albedo at 5 m varies from 0.15 to 0.65, with the lower values resulting from flights where the HELiX started above a dark surface (melt pond) and the higher values representing flights where the HELiX started

above snow-covered ice surfaces. When the aircraft altitude is increased, measured albedo values increase/decrease as the heterogeneity of surface features observed by the downward-facing pyranometer increases. As discussed above, this change in measured albedo results from the fact that the pyranometer measurements of reflected surface radiations follow the relationship of the cosine function of the radiation incident angle, corresponding to a weighted average of the surface albedo. It means that features directly below the platform carry greater influence on the measured signal than features at the edge of the instrument field of view. To allow for cross-flight comparison despite grid flights being conducted at different altitudes, these flights are separated into 3 categories: grid flights with altitude higher than 18 m, grid flights with altitude between 12 m and 18 m, and grid flights with altitude below 12 m. These 3 categories are distinguished with markers in **Figure 4a** and **b** and are displayed in individual plots in **Figure 5**.

Distributions of albedo are obtained for each grid flight as introduced in **Figure 3a** and **b**, with the results shown

in **Figure 5b–d**. In **Figure 5b**, albedo distributions are shown for flights with a mean grid altitude below 12 m. The distribution peak represents the albedo values with the maximum frequency of occurrence for a grid flight. Earlier flights registered a main peak albedo around 0.5–0.6 (more bright surfaces), while later flights showed a peak between 0.2 and 0.4 (more dark surfaces as melt ponds). The overall range of albedo values appeared to be the same for this 12 day-period for grid flights below 12 m with asymmetric bimodal distributions. Note that the flights took place on consecutive days and in diffuse conditions. However, as the floe underwent abrupt changes, the albedo correspondingly varied from brighter to darker values over the area of the HELiX flights. The distributions of albedo also captured the time evolution of the sea ice as more melt ponds appeared or became larger on the MOSAiC floe. This evolution of albedo is expected but is nonetheless interesting to notice in this data, as the flights in **Figure 5b** did not take place over the same area, but rather at different locations as introduced in **Figure 1** with the satellite image.

As seen in **Figure 4a**, flights between 12 and 18 m were more separated in time and fewer in number than flights below 12 m. In **Figure 5c**, for grid altitude between 12 and 18 m, the range of each distribution was narrower than in **Figure 5b** (except for FL34), and distribution bounds varied with flight. While flights below 12 m seem to capture a broader range of albedos (resulting from better resolution of independent surface features) along with an asymmetric bimodal distribution, albedo from flights higher than 12 m present only 1 mode. The case of FL34 took place over a different ice floe (noted previously); therefore, it is hard to compare directly with other distributions. This case conveys information about the albedo in the marginal ice zone, showing a bimodal distribution with a large hump between 0.2 and 0.6 corresponding to ocean/melt pond albedo and a sharper peak around 0.65 for snow/bare ice. Otherwise, the shape of these distributions can be explained by the flight altitude, whereby hemispheric upwelling shortwave irradiances were implicitly averaged over a larger area, and albedo of individual surface features started to blend. These altitude-dependent observations are supported by the profile flights shown in **Figure 5a**.

Comparisons are more difficult using grids flown at altitudes higher than 18 m (**Figure 5d**) since there were only 3 flights. FL04 and FL05 occurred at the end of June when melt ponds were already visible on the ice floe, and FL32 took place after the MOSAiC floe disintegrated. FL32 was clearly above the ocean, with only the presence of a few pieces of ice. FL04 and FL05 took place the same day when the team was still adjusting the grid parameters (dimensions, velocity, overlap). Therefore, the HELiX covered larger areas compared to other grid flights. This could explain why 2 modes for melt pond and snow/bare ice are visible in the distribution despite the higher flight altitude. Thus, to complement surface information from albedo measurements, it is meaningful to investigate melt pond fraction associated with each flight.

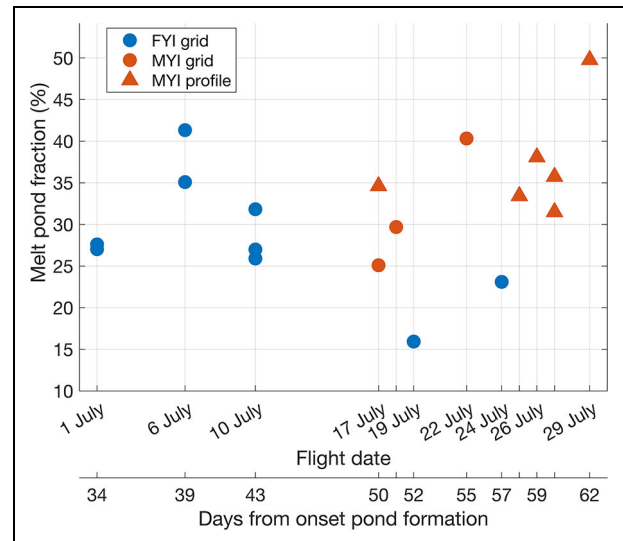


Figure 6. Melt pond fraction from the HELiX. Melt pond fraction from the orthomosaics as a function of the flight date and the days from the onset of melt pond formation.

3.2. Melt pond fraction

Using the method described in Section 2, melt pond fraction is calculated for each horizontal grid and vertical profile flight. Results are displayed in **Figure 6**, where blue dots correspond to grid flights executed over FYI and red dots corresponding to grid flights over MYI. The triangles represent profile flights over the MYI, with the orthomosaic images from those flights covering a larger area than for grid flights, but with a lower resolution. A summary of the flight types, flight altitudes, image areas, and image resolutions can be found in Table S1. The last 4 grid flights of the campaign (FL27, FL30, FL32, and FL34) did not provide reliable orthomosaic images. These flights had a higher presence of dark ocean, which makes it difficult for the software to stitch images together, and higher ice drift velocity, which inhibited the necessary 80% overlap between images. Therefore, results from these 4 flights cannot be included in the melt pond fraction analysis. Melt pond fraction from the viable HELiX flights ranged from 15% to 50%. To compare with previous melt pond observations (e.g., Polashenski et al., 2012; **Figure 1**), the days since the first onset of ponding on the MOSAiC floe (observed via satellite imagery on May 28, 2020) are added to the x-axis in **Figure 6**. When comparing with previous campaigns including measurements after 34 days of melt, a similar range of melt pond fraction was observed. Nonetheless, as noted in previous studies, melt ponds are highly variable and dynamic. Because of the difference between the measurement year and the locations, observations of melt pond fraction span a large range. The method of measurements also impacts the results particularly the spatial resolution, as introduced in **Figure 7**.

Few satellite images were collocated in time and space with the HELiX flights as a result of frequent and dense cloud cover. However, SkySat satellite images were collected on July 7 and 22, 2020, that can be compared with FL07 on July 6 and FL19 on July 22 to provide context

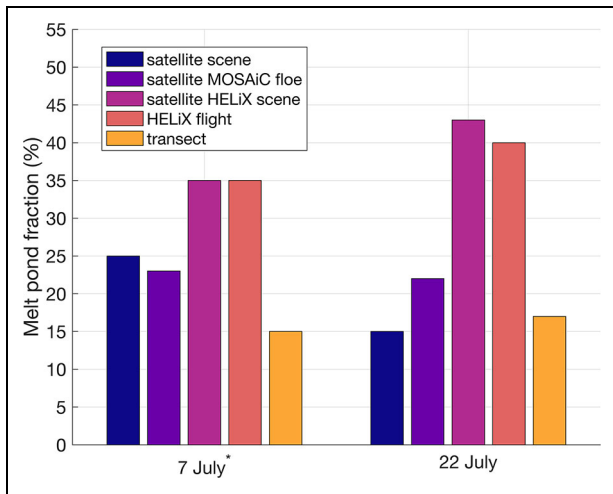


Figure 7. Comparison of melt pond fraction. Melt pond fraction from SkySat satellite images (Wright et al., 2021), the HELiX orthomosaics, and the transect data (Webster et al., 2022). *The HELiX flight occurred on July 6.

for the HELiX flights. **Figure 7** illustrates the variation of melt pond fraction obtained from these case comparisons when considering different areas within a day. Surface identification maps from Wright et al. (2021), based on the SkySat satellite images, are used to compare with the HELiX flight orthomosaic. The full satellite scenes correspond to areas of 86 and 80 km² for July 7 and 22, respectively. Zooming in to the MOSAiC floe and areas corresponding to the HELiX flights, the MOSAiC floe corresponds to an area of 1.65 km² and the HELiX flights to 0.01 and 0.02 km². There is good agreement between the satellite-based estimation of melt pond fraction in the HELiX flight area (**Figure 7** “satellite HELiX scene”) and the values obtained from the HELiX orthomosaic (**Figure 7** “HELiX flight”). This agreement is reached despite the different resolutions of the sensors and the independent melt pond fraction calculation methods. However, it can be noticed that larger areas show a lower melt pond coverage compared to the HELiX flights as multiple melt pond regions and multiple floes are captured in the satellite images. Transect measurements are from Webster et al. (2022) and provide yet another estimate of melt pond fraction, with these values being notably lower than the satellite- and HELiX-based observations. The transect represents a 3-km survey of manual measurements along the MOSAiC floe edge and reports a lower melt pond coverage by 5% on average compared to satellite retrievals in June and July (Webster et al., 2022). This difference can be explained as melt ponds near the edge of the floe may drain laterally earlier than ponds centered on the floe, which are constrained by high surface relief.

Figure 6 also shows a decrease in melt pond fraction over the FYI toward the later portions of the campaign. This decrease results from a significant pond drainage event that occurred during the period of measurements on July 11–13. More details on this event can be found in

Webster et al. (2022). As confirmed by **Figure 6**, MYI covered by the HELiX flights was less impacted by this drainage event and experienced a continued increase of pond coverage after July 13. Flights over the FYI were also close to the edge of the floe and might therefore have been impacted by lateral drainage similarly to the transect data. The observed drainage event was similar to the one observed during the 2011 Applied Physics Laboratory Ice Station, which also featured a significant decrease of melt pond coverage over the FYI while pond fraction continued to increase over MYI (Webster et al., 2015). A more complete description of the evolution of melt ponds and the drainage events can be found in Niehaus et al. (2023) based on Sentinel-2 satellite images. The MOSAiC floe presented a higher melt pond fraction compared to the surrounding floes until mid-July. The satellite images also captured the main transformation of the floe. Before drainage, large and distinct ponds were visible. After drainage, ponds appeared small and interconnected, darkening the floe surface, an appearance that was also reinforced by sediments embedded in the ice and then exposed as the melt progressed (Lei et al., 2022; Webster et al., 2022; Niehaus et al., 2023). Thus, detailed quantification of the drainage event using HELiX data should be conducted with caution, as HELiX flights were not designed to precisely monitor the same ponds over time. Because of the continuously drifting nature of the ice during HELiX flights, overlap of individual images used to create the orthomosaics was often less than anticipated, resulting in a lack of data between the legs of the grid flights, adding a layer of uncertainty to melt pond fractions based on the orthomosaics from HELiX flights.

3.3. Link between melt pond fraction and profile of albedo

The HELiX UAS, with collocated but independent measurements of melt pond fraction and albedo, provided an opportunity to quantify the impact of the sea ice features on albedo. Because of the hemispheric nature of most broadband pyranometers, the size of the surface features being observed and the altitude from which measurements are taken have a significant impact on the measured irradiance. Previous studies to understand the influence of melt pond evolution on surface albedo have demonstrated this influence, including attempts to suspend pyranometers at 15 m above the surface to cover a larger area than measurements obtained at the normal 2 m height (Langleben, 1968, 1969). Surface albedo has also been investigated as a function of aircraft altitude for the transition between open ocean and land (Jakel et al., 2013). The current HELiX UAS dataset helps to consolidate knowledge on the impact of melt pond fraction on observed albedo as a function of measurement altitude.

Consider the orthomosaic from FL22 on July 25 shown in **Figure 8**. Here, melt pond fraction is calculated for a sequence of concentric surface footprints, with the footprint increasing in radius by steps of 5 m, and 2 cases where the center point of the footprint includes either a melt pond (**Figure 8b**) or bare sea ice surface

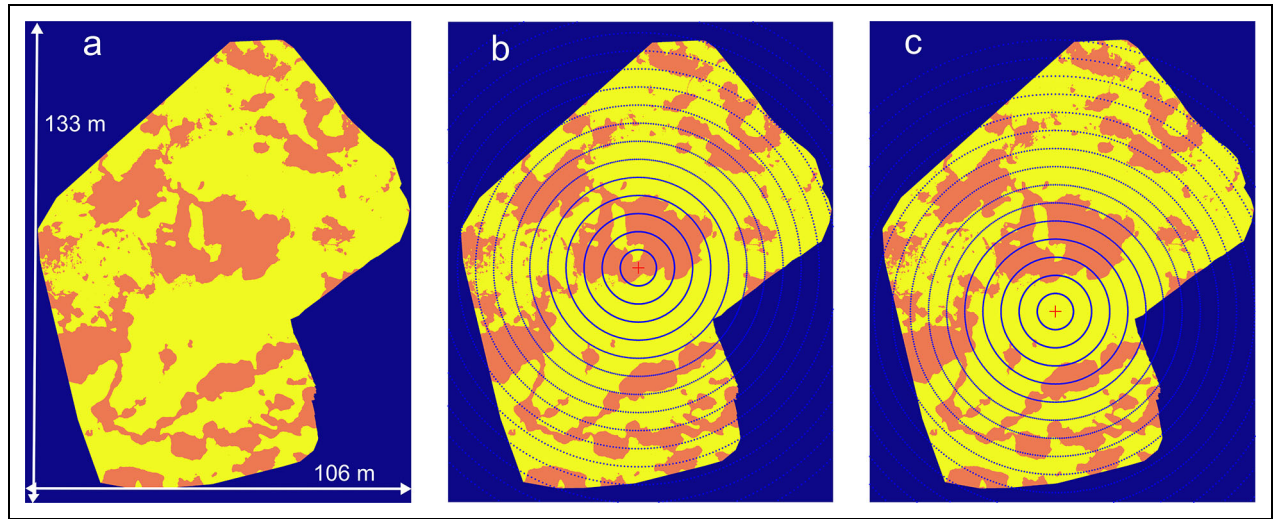


Figure 8. Surface type identification from the HELiX orthomosaics. (a) Surface type identification map for profile FL22 (July 25, 2020), division of the map in (b) circles centered above melt pond, and (c) circles centered above snow/bare ice.

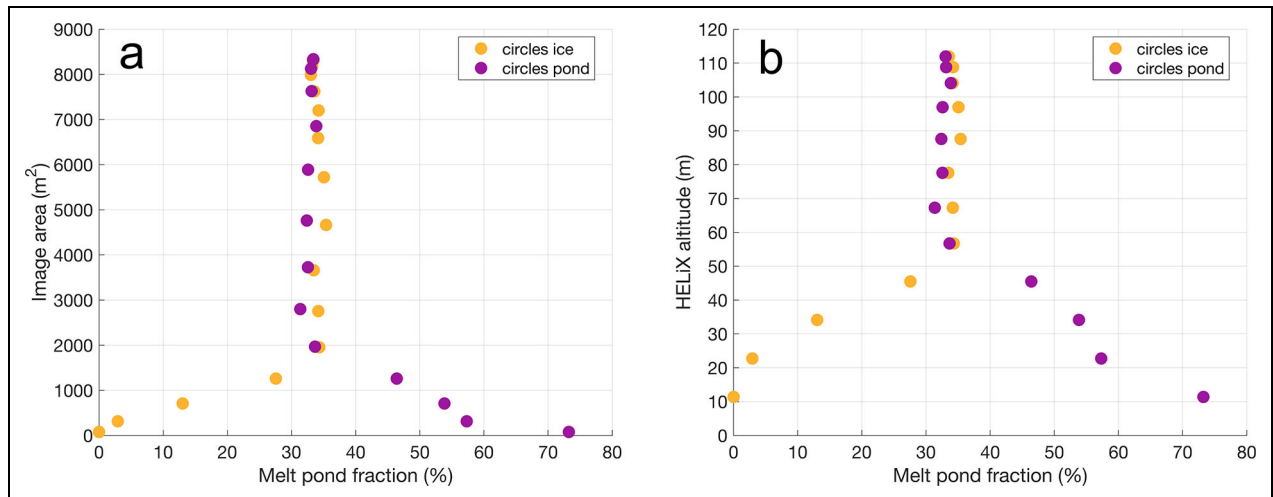


Figure 9. Melt pond fraction as a function of image area and HELiX altitude. (a) Melt pond fraction obtained for each division from Figure 8 function of the area of each division for the HELiX orthomosaic FL22 on July 25, 2020. (b) Melt pond fraction obtained from increasing circles function of the HELiX UAS altitude calculated with the camera field of view.

(Figure 8c). Figure 9 shows the extent to which melt pond fraction decreases or increases as these footprints grow, until the footprint encompasses the entire orthomosaic and the melt pond fractions of these 2 sequences converge to each other. Interestingly, the derived melt pond fraction sequences closely approximate the convergence value for the entire image at a footprint much smaller than the scale of the entire orthomosaic. The footprint scale at which this approximate convergence occurs we refer to as the “aggregate-scale” (Perovich, 2005). For the 6 profile flights available from July 17, 25, 26, 27, and 29, the aggregate scale for melt pond fraction varies between 2,000 and 3,000 m². All of the profile flights conducted by the HELiX during MOSAiC took place in the same sector of the MOSAiC ice floe, explaining the limited variability found in the aggregate scale. Note that the

aggregate scale of melt pond fraction is dependent on the dimensions of the studied area. Wright and Polashenski (2018) analyzed the images of Arctic sea ice up to 1,000 km² and found an aggregate scale of melt pond fraction on the order of several tens of square kilometers. For the HELiX flights, the orthomosaic dimensions are smaller than 80,000 m² and provide a high-resolution analysis for only limited parts of the MOSAiC floe. To further link this aggregate scale of melt pond fraction with the observed surface albedo in Figure 9b, a HELiX altitude is estimated based on the sensor footprint defined by the circles in Figure 8 and the field of view of the multispectral camera (47.5° horizontal and 35.4° vertical). Figure 9b shows the aggregate scale for FL22 corresponding to the HELiX altitude around 55 m when melt pond fraction converges toward the same value.

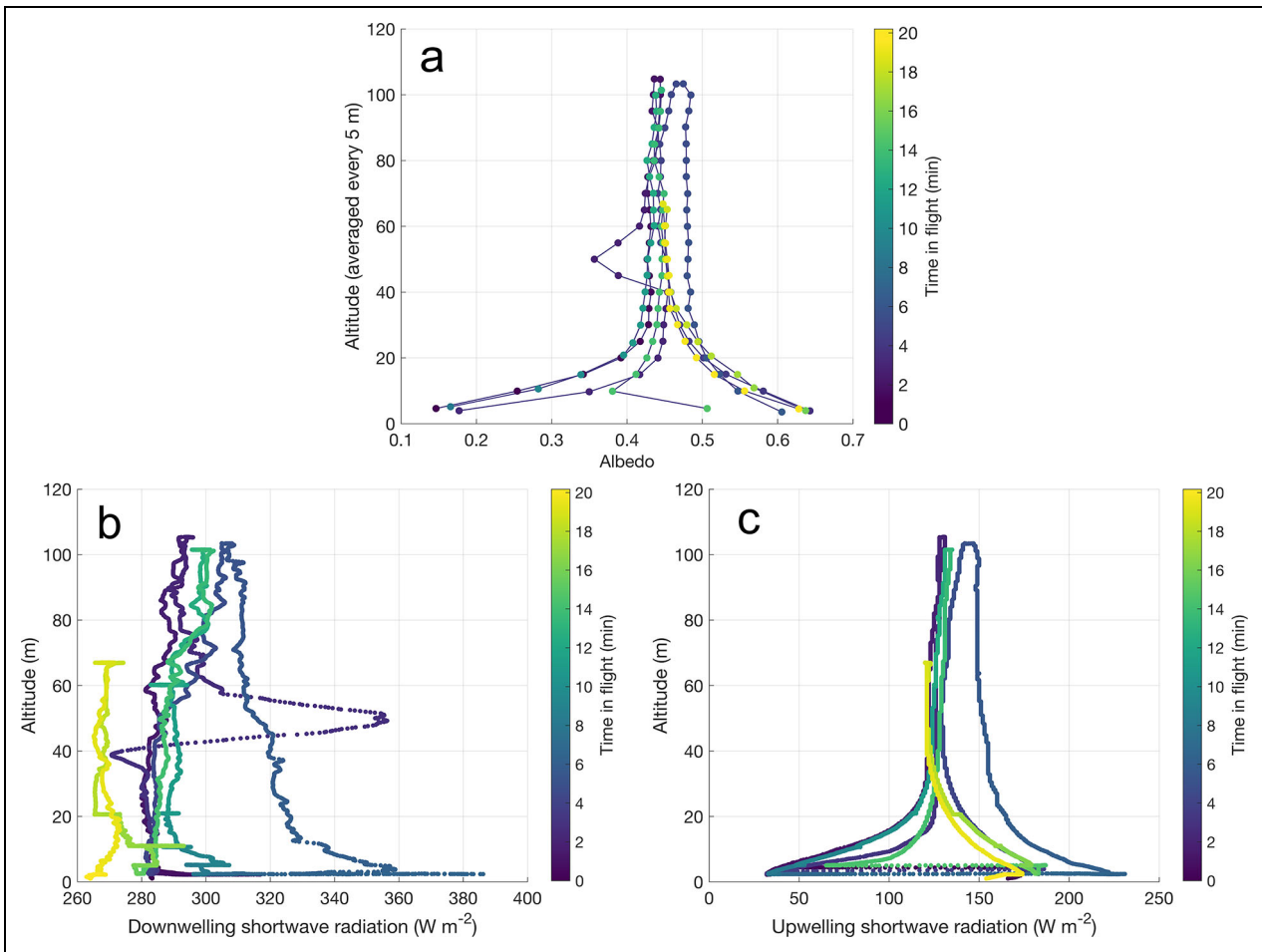


Figure 10. Measurements from the HELiX pyranometers. (a) Measured albedo from pyranometers for the HELiX profile FL22 on July 25, 2020. Albedo is vertically averaged over 5-m intervals. (b) Downwelling shortwave radiation from the top pyranometer for FL22. (c) Upwelling shortwave radiation from the bottom pyranometer for FL22.

As expected, the vertical profile of surface albedo obtained from the HELiX pyranometers takes on a similar shape to that of the melt pond fraction with an increasing footprint scale. **Figure 10a** shows measured albedo as a function of altitude for FL22, the HELiX flight shown in **Figures 8** and **9**. To reduce high-frequency variability, measured albedo was averaged over 5-m vertical intervals. During the flight, the HELiX climbed multiple times, starting above either a melt pond (albedo < 0.2) or snow/bare ice surface (albedo > 0.6). The constituent downwelling and upwelling shortwave irradiances are additionally shown in **Figure 10b** and **c**. These help to explain the observed decrease in albedo between 40- and 60-m altitude, and the increased albedo values associated with one of the early profiles: because FL22 took place with a thin, low cloud/fog layer in place, there were periods when the cloud dissipated enough to result in a clear sky or thin cloud condition at the height of the UAS, increasing the downwelling irradiance to values exceeding 340 W m^{-2} . In some cases, this resulted in a fog-top albedo value, while in other cases, this resulted in a clear-sky, direct radiation albedo value, rather than one associated with diffuse incoming solar

energy. For low sun angles, light scattering from the surface is not uniform because the scattering phase function of ice and water have a strong forward-scattering component. Except for the first 2 descents with these varying sky conditions, albedos generally merged to a common value 50–60 m above the surface. Similarly, the melt pond fraction approached an aggregate scale once the UAS reached an altitude of approximately 55 m (**Figure 9b**).

4. Sensitivity analysis

To investigate the representativeness of the albedo profiles derived from the HELiX UAS for the rest of the ice floe around the MOSAiC domain, SkySat satellite imagery from July 22, 2020, was used. For this evaluation, the HELiX data are first compared to information derived from the SkySat imagery for the HELiX flight locations. After validation, different points on the MOSAiC floe, including profile locations over both melt pond and snow/bare ice, were selected to obtain virtual vertical profiles of albedo and study the link between the size and density of surface features and the vertical variation of measured surface albedo.

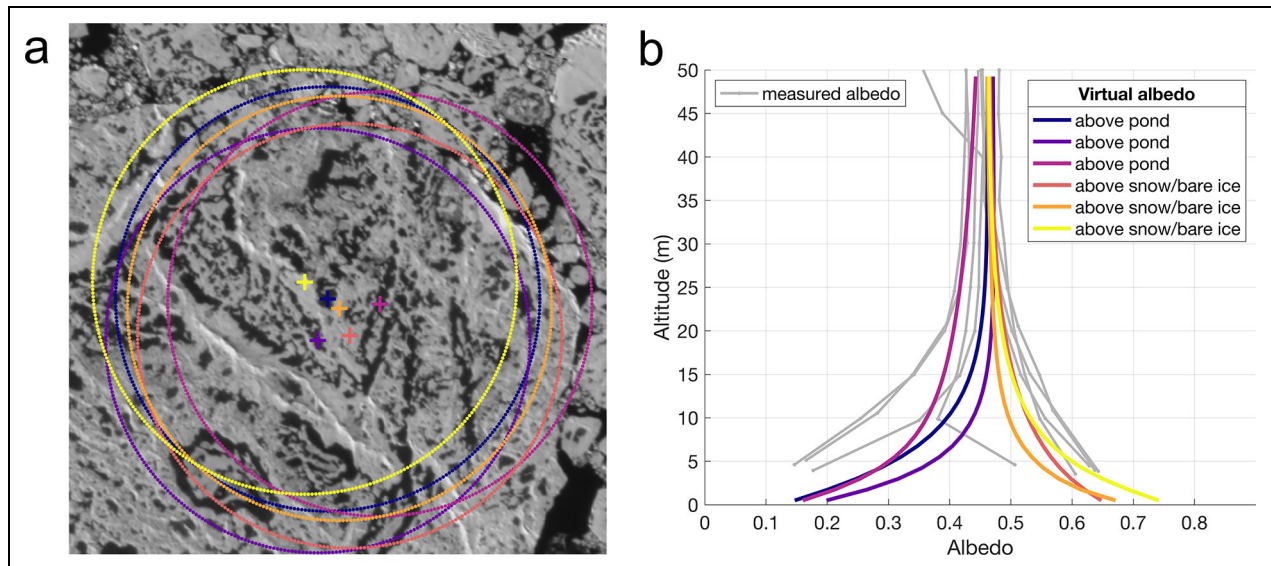


Figure 11. SkySat satellite image on July 22, 2020. (a) Selected area of the HELiX FL22 flight (Imagery © 2022 Planet Labs Inc.); crosses represent the starting point of the virtual profiles of albedo, either above pond or snow/bare ice; circles represent the downward-facing pyranometer footprint at 50 m (diameter/height = 10). (b) Measured albedo profiles in gray from the HELiX flight FL22 on July 25, 2020, for altitudes between 0 and 50 m and virtual albedo profiles based on satellite image; profiles initiated over snow/bare ice and melt pond correspond to the same color cross and circle in (a).

4.1. Model to reproduce vertical profiles of UAS-measured albedo from satellite images

The analysis using the SkySat satellite image (July 22, 2020) was initially centered on the location of the MOSAiC floe where the July 25 HELiX profile flight (FL22) took place. A preliminary grayscale calibration of the satellite image was applied, assigning pixel values between 0 and 255 to represent albedos ranging from 0.05 (open ocean) to 0.9 (bright snow). This simple method rescales linearly the range of albedo for each satellite image (July 7 and 22, 2020) based on the pixel values. This calibration does not intend to be exhaustive, but rather designed for an initial comparison with the HELiX measured albedo. Six locations above ponds and snow/bare ice were selected, as represented by the colored crosses in **Figure 11a**. Specifying a radiation view factor of 0.95 for a downward-pointed pyranometer (Sailor et al., 2006), the virtual footprint corresponding to the observation was estimated as a function of height, represented as dotted circles in **Figure 11a**. The process for deriving these footprints is discussed in detail in Supplemental Material with Figure S2 (Langleben, 1968; Siegel and Howell, 1981; Roberts et al., 2008). Using the calculated sensor footprint and scaled surface albedo from SkySat imagery, virtual profiles of measured albedo are calculated between the surface and 50 m (**Figure 11b**). For comparison, in gray in **Figure 11b**, the measured albedo profile from FL22 conducted with the HELiX is shown for the same altitude range. The calculated and measured albedo profiles show similar shapes, with converging values up to a given altitude, defined as the merging altitude. This comparison shows that virtual albedo profiles derived from the SkySat image reproduce realistic changes in measured albedo with altitude, validating the

model for constructing virtual albedo profiles from satellite-derived images.

4.2. Study of variation of surface feature sizes and corresponding albedo with altitude

The area sampled during FL22 included a relatively narrow distribution of melt pond sizes (**Figure 11a**). To better understand the influence of a broader distribution of melt pond scales on such measurements, a larger section of the SkySat satellite image on a different date is used (July 7, 2020). During this time, large melt ponds were present on the MOSAiC floe and surrounding sea ice before the drainage event that occurred a few days later on July 11, 2020 (**Figure 12a**). To evaluate the merging altitudes obtained when starting over surface features of different sizes, multiple melt ponds on the floe were selected as starting points over which to calculate albedo profiles (blue crosses in **Figure 12a**). In **Figure 12b**, crosses are also displayed over the same melt ponds as in **Figure 12a**, but this time, the crosses are color-coded by area, with dark blue representing the largest pond and orange the smallest. Additionally, 7 locations were selected over snow/bare ice surfaces and represented by markers with different shapes in **Figure 12b**.

Applying the same method that was used in Section 4.1, we calculate albedo profiles from SkySat imagery on July 7, 2020, before drainage, starting over a variety of different surface features. Based on the methods outlined in Supplemental Material (Figures S3 and S4), a maximum altitude of 400 m and diameter/height ratio (DHR) of 10 was employed. Results are presented in **Figure 13**. Nonetheless, as the footprint diameter for a downward-pointing sensor increases with altitude, orthomosaic images should generally be large enough to encompass

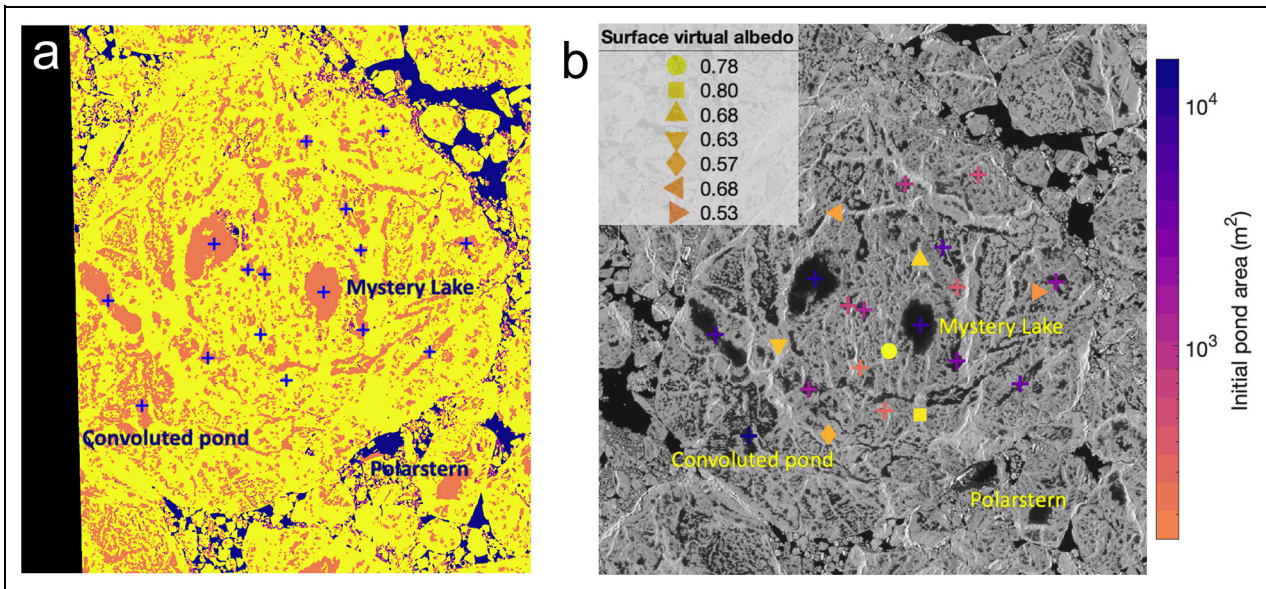


Figure 12. Satellite image on July 7, 2020. (a) Surface map classification (Wright et al., 2021), the blue crosses are centered on 16 selected ponds. (b) SkySat satellite image (Imagery © 2022 Planet Labs Inc.) with crosses centered on selected ponds color-coded by initial pond area and markers with different shapes placed on 7 snow/bare ice surfaces color-coded by surface virtual albedo. The different symbols correspond to results presented in **Figure 13b**.

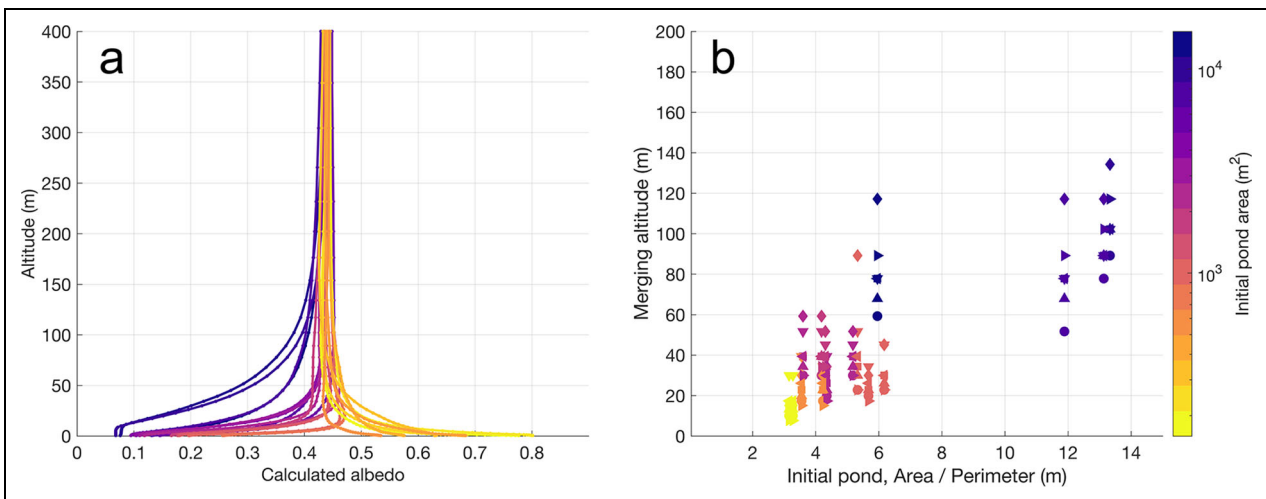


Figure 13. Virtual profiles of albedo and corresponding merging altitudes. (a) Calculated profiles of albedo started above the 16 selected ponds and the 7 snow/bare ice surface from **Figure 12b**. (b) Merging altitude obtained from the difference between albedo profiles started above pond and snow/bare ice as a function of melt pond area and melt pond perimeter (DHR = 10). The difference is calculated between each profile started above pond with each profile started above snow/bare ice. Therefore, the markers correspond to merging altitude with one of the profiles initiated over the corresponding marker in **Figure 12b**.

the footprint at the maximum flight altitude. In practice, there are various reasons that a lower DHR might need to be used, including a lack of images to complete the orthomosaic, the point of interest being near an image border, the orthomosaic being too small, or cloud cover. Therefore, Figure S5 additionally provides results using DHRs of 6 and 4 to highlight the impact of a reduced footprint on this analysis. The spread of merging altitudes (i.e., altitude above which the albedo is representative of the floe scene, see example below) increases as DHR decreases, as shown by the more transparent markers in Figure S5.

The profiles of albedo calculated above the selected points are presented in **Figure 13a** for a footprint DHR of 10. Albedo varied at the surface from values lower than 0.1 for dark melt ponds to values exceeding 0.8 over very bright surfaces. At 400 m, the 23 profiles (16 ponds and 7 snow/bare ice) merged toward a representative albedo value, 0.439 ± 0.004 . As expected, profiles initiated over larger ponds converged toward the representative albedo value at higher altitudes than those starting over above small structures. To quantify the altitude above which albedo values are representative of the broader floe, the

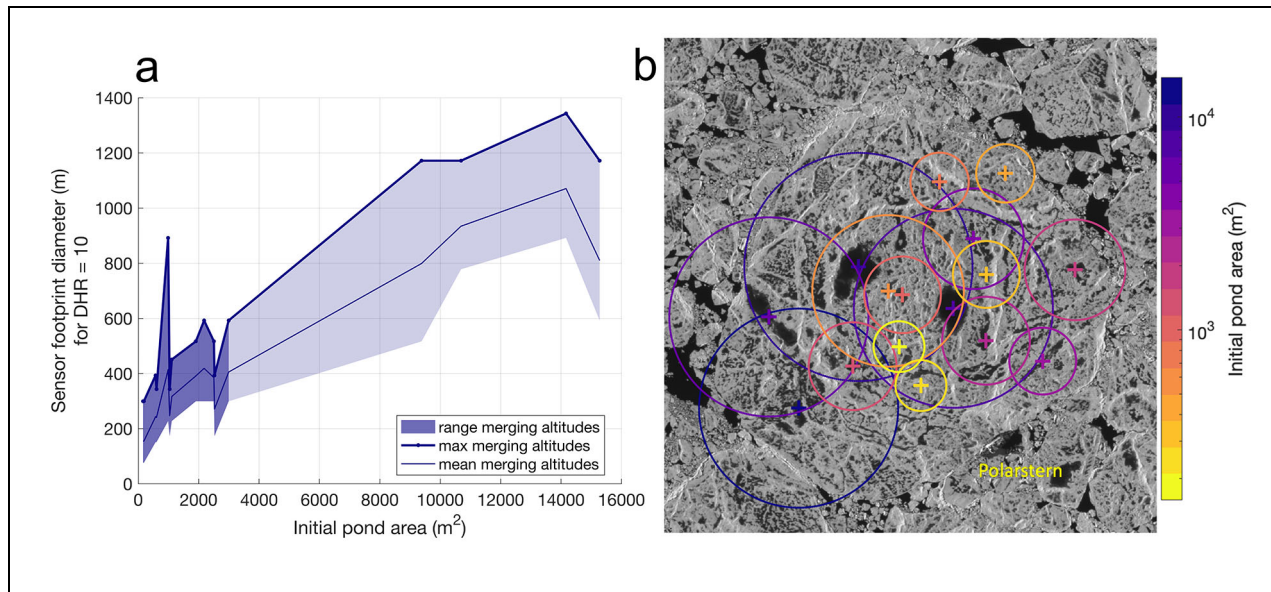


Figure 14. Pond areas as a function of the sensor footprint diameter. (a) Initial pond areas as a function of the sensor footprint diameters calculated at the merging altitudes (Figure 13b) for DHR = 10. (b) SkySat satellite image on July 7, 2020 (Imagery © 2022 Planet Labs Inc.) with circles drawn around each nadir origin point with the diameter obtained at the maximum merging altitude (DHR = 10).

difference between profiles initiated over ponds and those initiated over snow/bare ice was calculated. The merging altitude is defined as the altitude, where the difference between profiles is less than 10% of the difference in albedo at the surface. For example, surface albedo for “Mystery Lake” is calculated to be 0.07, and the value associated with the snow/bare ice surface represented by a circle marker in Figure 12b is 0.78. Then, the surface albedo difference is 0.71, and the merging altitude for the profiles started above these 2 points is defined as the altitude where the difference between the 2 profiles is lower than 0.071, which in this case occurs at 77.82 m (Figure 13b). This calculation is repeated for all of the profile pairs initiated over ponds with 1 profile in the pair initiated over a single snow/bare ice location, for example, the circle in Figure 12b, leading to merging altitudes displayed with circle markers in Figure 13b. Then, merging altitudes are calculated between the pond profiles and another profile initiated over snow/bare ice with a different brightness and represented by another marker in Figure 12b, leading to a display of merging altitudes with the corresponding marker in Figure 13b.

To better account for the influence of the pond shape complexity on merging altitude, the calculated merging altitudes are plotted as a function of the ratio between melt pond area and pond perimeter (A/P). This ratio is higher for larger, coherent, and symmetric ponds, and smaller for ponds with complex, curving boundaries, like the pond observed at the bottom left of the MOSAiC floe (Figure 12b). While this calculation offers additional insight into the influence of pond complexity, the albedo merging altitudes are found to primarily be impacted by the pond area, with complexity playing a secondary role (e.g., the convoluted pond shows a lower A/P ratio than Mystery Lake, but with a similar area. Nonetheless,

merging altitudes for this pond are still in the same range than Mystery Lake, see Supplemental Figure S6).

Merging altitude is not only found to change with pond area and perimeter but also with snow/ice surface brightness. The spread in merging altitude results from different profiles being initiated over areas with various brightness, and this feature is represented by the marker shapes in Figure 13b. This spread is largest for ponds with large surface areas ($>10,000 \text{ m}^2$) and smaller for ponds smaller than 200 m^2 . In other words, while pond size is the primary driver of the derived albedo as a function of height, the surrounding sea ice surface can also play a role in driving albedo gradients with height. As expected, the merging altitude is greater for profiles starting over larger melt ponds.

Figure 14 shows sensor footprint diameters at the calculated merging altitudes for 16 selected ponds with DHR set to 10. Note that ponds were manually selected to span a range of scales on the MOSAiC floe. Most pond areas are below $4,000 \text{ m}^2$ and the maximum footprint remains smaller than circles with 600 m diameter. To visually represent these footprints, the maximum merging altitude for each pond is selected and circles with the corresponding diameters are marked in Figure 14b. Except for the 4 large ponds present before drainage, footprints are typically on the order of 300–600 m diameter at the date of the satellite image (July 7, 2020). These preliminary results should be further completed with a spatial and temporal statistical analysis for more thorough conclusions.

The above analysis allows us to estimate HELIX flight altitudes required to have the measured surface albedo be representative of the broader MOSAiC floe. Below the calculated merging altitude, albedo measurements are biased by the surface feature directly beneath the sensor.

This satellite-centric analysis offers a method to estimate the height and the footprint diameter, at which a representative surface albedo can be measured. The analysis also provides new insight on spatial heterogeneity in albedo in relation to melt pond coverage and geometry from a spatial scaling perspective. These results are relevant for evaluating and developing model parameterizations that represent melt ponds, as well as their linkages to surface albedo, as satellite-based sensors can provide much broader coverage than individual UAS can, except for in cloud-covered regions.

5. Discussions and summary

As part of the MOSAiC expedition, the HELiX UAS was operated over the central Arctic sea ice during summer 2020. Different flight patterns were conducted, including horizontal gridded flights (maximum 370 m × 335 m) and vertical profiles (generally up to 100 m). Most HELiX flights took place under diffuse light conditions, either under low clouds or in a layer of fog. From this data set, surface albedo was calculated from the onboard pyranometers and melt pond fraction was obtained from orthomosaic images generated using the HELiX-collected photographs. This study provides the following insights on the temporal and spatial evolution of the MOSAiC ice floe, complementing other albedo and melt pond fraction measurements that took place during MOSAiC.

During grid flights, data from the onboard pyranometers captured changes in surface albedo associated with different surface features. Data collected at different flight altitudes showed that grid flights below 12 m captured asymmetric bimodal distributions of albedo, with maximum values observed over bright surfaces and lower values representing melt ponds and open ocean. Grid flights executed at altitudes above 12 m documented a narrower distribution of albedo and generally only featured a single mode. Differences in the shape of the distributions can be explained by the increased blending of surface features with flight altitude. Therefore, lower altitude grids are better for capturing the full range of individual surface albedo values over a given flight area.

These surface albedo results are complemented by surface imagery from the multispectral camera to calculate melt pond fraction under the HELiX. The method developed to identify melt ponds from the orthomosaic images agrees well with similar methods used for satellite images (e.g., Wright et al., 2021). HELiX flights additionally provided information about the time evolution of the MOSAiC floe, capturing drainage events over the FYI on July 10–13, and extending the information from other albedo measurements collected as part of MOSAiC, such as the albedo transect data (Webster et al., 2022) and satellite images (Wright et al., 2021).

HELiX profile flights contributed to understanding the impact of altitude on the measurement of albedo. Using data from the HELiX pyranometers and multispectral camera together with imagery from the SkySat satellite, a relationship was derived between the dimensions of the surface features under a given profile and the variation of albedo with altitude. Larger pond sizes under the center

of a profile result in a higher albedo merging altitude. However, the results shown here suggest that most spatial variability in albedo across the MOSAiC ice floe occurred on scales less than about 300–600 m. These results should be considered carefully when comparing albedo measurements across a variety of spatial scales (e.g., satellite vs. surface-based observations) and should be leveraged for the planning of future field efforts to document surface albedo across complex surface types. Satellite images could be used to further validate existing UAS albedo measurements, qualifying those that have sufficient height to be representative. Or, satellite images could be used in flight planning for new measurements to ensure they will be taken from representative heights.

Deployment of the HELiX UAS during leg 4 of the MOSAiC expedition resulted in the collection of valuable data of surface albedo (Calmer et al., 2021; Hamilton et al., 2021). Future deployments of the HELiX will benefit from this experience, and future data sets collected by airborne platforms will be strengthened from this analysis. Future work to analyze the HELiX data will include attempts to calibrate the orthomosaic images to obtain pixel-based albedo measurements and support the derivation of a full distribution of surface albedo for orthomosaic imagery. The HELiX could be redeployed to sea ice and other surfaces, extending this work and that of others (e.g., Tschudi et al., 2007; de Boer et al., 2016; Burkhart et al., 2017). Observational data collected by low-flying UAS can be extremely valuable in filling in gaps related to satellite sensing in cloudy areas and/or reduced variability as observed by higher flying crewed aircraft. Collocated measurements of albedo, light transmittance, and sea ice mass balance were completed during MOSAiC (Nicolaus et al., 2022), and future work is underway to connect these different optical parameters measured during summertime of 2020 to understand the fate of solar energy. The use of the HELiX data to assess and improve surface models supporting weather and climate prediction is envisioned, and future work is planned in this direction. Interdisciplinary analysis will ultimately help advance understanding of the ice-ocean albedo feedbacks and improve prediction of weather and climate in the Arctic region.

Data accessibility statement

The quality-controlled and synchronized data set used in this analysis are available through the Arctic Data Center from the onboard data logger (Calmer et al., 2021; <http://dx.doi.org/10.18739/A22J6857H>) and from the multispectral camera (Hamilton et al., 2021; <http://dx.doi.org/10.18739/A2T727H3V>). The surface map classification is obtained from Wright et al. (2021) and SkySat Imagery is available from Planet Labs, Inc. (<http://dx.doi.org/10.18739/A2833N04M>). Data from the ASFS50 are available at the Arctic data center (Cox et al., 2021; <http://dx.doi.org/10.18739/A2445HD46>). The transect data are available on PANGAEA (Itkin et al., 2021; <https://doi.pangaea.de/10.1594/PANGAEA.937781>). Diffuse fraction is obtained from Atmospheric Radiation Measurement user facility at <http://dx.doi.org/10.5439/>

1411966; <http://dx.doi.org/10.5439/1411966>; and <http://dx.doi.org/10.5439/1608608>.

Supplemental files

The supplemental files for this article can be found as follows:

Supplemental material.docx

Acknowledgments and funding

The data described in this manuscript were collected through financial support from the US National Science Foundation (OPP 1805569) as part of the international Multidisciplinary drifting Observatory for the Study of the Arctic Climate (MOSAiC) with the tag MOSAiC20192020. We thank all persons involved in the expedition of the Research Vessel *Polarstern* during MOSAiC in 2019–2020 (AWI_PS122_00). CJC received support from the U.S. National Oceanic and Atmospheric Administration Global Ocean Monitoring and Observing Program (FundRef: <https://doi.org/10.13039/100018302>). MDS was supported by the National Science Foundation (OPP-1724551), U.S. Department of Energy (DE-SC0021341), and NOAA Cooperative Agreement (NA22OAR4320151). MAW conducted this work under NASA's New (Early Career) Investigator Program in Earth Science (80NSSC20K0658) and the National Science Foundation (2138786). We thank Dr. Greg Roberts for his insights in the calculation of albedo profiles based on the sensor altitude. We appreciate feedback provided by Dr. Gary Wick (NOAA-PSL). All SkySat Imagery is the copyright of Planet Labs, Inc. (2022).

Competing interests

The authors declare that they have no competing interests.

Author contributions

RC is the primary author for this manuscript. GdB is the lead PI for the project that resulted in the collection of these data. JJC and DL are co-PIs for this project and contributed to the design, planning, and execution of the campaign. DL and JH contributed to the preparation of aircraft and instrumentation for the field campaign. RC and JH participated in the collection of the HELIX data in the field during the MOSAiC campaign. GdB, RC, JH, and DL all contributed to the processing and analysis of data. MDS and CJC provided advice on albedo analysis. MAW and NW provided the SkySat satellite multispectral image from Planet Labs, Inc., surface classification maps, and transect results. All authors contributed to the review, editing, and writing of the manuscript.

References

- Buckley, EM, Farrell, SL, Duncan, K, Connor, LN, Kuhn, JM, Dominguez, RT.** 2020. Classification of sea ice summer melt features in high-resolution IceBridge imagery. *Journal of Geophysical Research: Oceans* **125**(5): e2019JC015738. DOI: <http://dx.doi.org/10.1029/2019JC015738>.
- Burkhart, JF, Kylling, A, Schaaf, CB, Wang, Z, Bogren, W, Stordvold, R, Solbø, S, Pedersen, CA, Gerland, S.** 2017. Unmanned aerial system nadir reflectance and MODIS nadir BRDF-adjusted surface reflectances intercompared over Greenland. *The Cryosphere* **11**(4): 1575–1589.
- Calmer, R, de Boer, G, Hamilton, J, Lawrence, D, Borenstein, S, Cox, C, Argrow, B, Cassano, J.** 2021. HELIX uncrewed aircraft system data from the Multidisciplinary drifting Observatory for the Study of Arctic Climate (MOSAiC) campaign. Arctic Data Center. DOI: <http://dx.doi.org/10.18739/A22J6857H>.
- Comiso, JC, Parkinson, CL, Gersten, R, Stock, L.** 2008. Accelerated decline in the Arctic sea ice cover. *Geophysical Research Letters* **35**(1). DOI: <http://dx.doi.org/10.1029/2007GL031972>.
- Cox, C, Gallagher, M, Shupe, M, Persson, O, Solomon, A, Ayers, T, Costa, D, Hutchings, J, Leach, J, Morris, S, Osborn, J, Pezoa, S, Uttal, T.** 2021. Atmospheric Surface Flux Station #50 measurements (Level 1 Raw), Multidisciplinary drifting Observatory for the Study of Arctic Climate (MOSAiC), central Arctic, October 2019–September 2020. Arctic Data Center. DOI: <http://dx.doi.org/10.18739/A2445HD46>.
- de Boer, G, Calmer, R, Jozef, G, Cassano, JJ, Hamilton, J, Lawrence, D, Borenstein, S, Doddi, A, Cox, C, Schmale, J, Preußer, A, Argrow, B.** 2022. Observing the central Arctic atmosphere and surface with University of Colorado uncrewed aircraft systems. *Scientific Data* **9**(1): 1–17. DOI: <http://dx.doi.org/10.1038/s41597-022-01526-9>.
- de Boer, G, Dexheimer, D, Mei, F, Hubbe, J, Longbottom, C, Carroll, PJ, Apple, M, Goldberger, L, Oaks, D, Lapierre, J, Crume, M, Bernard, N, Shupe, MD, Solomon, A, Intrieri, J, Lawrence, D, Doddi, A, Holdridge, DJ, Hubbell, M, Ivey, MD, Schmid, B.** 2019a. Atmospheric observations made at Oliktok Point, Alaska, as part of the Profiling at Oliktok Point to Enhance YOPP Experiments (POPEYE) campaign. *Earth System Science Data* **11**: 1349–1362. DOI: <https://doi.org/10.5194/essd-11-1349-2019>.
- de Boer, G, Osborn, J, Cox, C, Intrieri, J, Borenstein, S, Dixon, C, Foscue, G.** 2019b. miniFlux data from Stratified Ocean Dynamics of the Arctic (SODA) campaign, Beaufort Sea and northern Alaska, 2018. Arctic Data Center. DOI: <http://dx.doi.org/10.18739/A2SJ19R18>.
- de Boer, G, Palo, S, Argrow, B, LoDolce, G, Mack, J, Gao, R-S, Telg, H, Trussel, C, Fromm, J, Long, CN, Bland, G, Maslanik, J, Schmid, B, Hock, T.** 2016. The Pilatus unmanned aircraft system for lower atmospheric research. *Atmospheric Measurement Techniques* **9**: 1845–1857. DOI: <https://doi.org/10.5194/amt-9-1845-2016>.
- Fetterer, F, Untersteiner, N.** 1998. Observations of melt ponds on Arctic sea ice. *Journal of Geophysical Research: Oceans* **103**(C11): 24821–24835. DOI: <http://dx.doi.org/10.1029/98JC02034>.

- Grenfell, TC, Perovich, DK.** 2008. Incident spectral irradiance in the Arctic Basin during the summer and fall. *Journal of Geophysical Research: Atmospheres* **113**(D12). DOI: <http://dx.doi.org/10.1029/2007JD009418>.
- Hall, A.** 2004. The role of surface albedo feedback in climate. *Journal of Climate* **17**(7): 1550–1568. DOI: [http://dx.doi.org/10.1175/1520-0442\(2004\)017<1550:TROSAF>2.0.CO;2](http://dx.doi.org/10.1175/1520-0442(2004)017<1550:TROSAF>2.0.CO;2).
- Hamilton, J, de Boer, G, Calmer, R, Lawrence, D, Argrow, B, Cassano, J.** 2021. HELiX Uncrewed Aircraft System data from the Multidisciplinary drifting Observatory for the Study of Arctic Climate (MOSAiC) campaign, multispectral imagery data. Arctic Data Center. DOI: <http://dx.doi.org/10.18739/A2T727H3V>.
- Inoue, J, Curry, JA, Maslanik, JA.** 2008. Application of Aerosondes to melt-pond observations over Arctic sea ice. *Journal of Atmospheric and Oceanic Technology* **25**(2): 327–334. DOI: <http://dx.doi.org/10.1175/2007JTECHA955.1>.
- Intergovernmental Panel on Climate Change.** 2021. *Climate change 2021: The physical science basis. Contribution of Working Group I to the Sixth Assessment Report of the Intergovernmental Panel on Climate Change* [Masson-Delmotte, V, Zhai, P, Pirani, A, Connors, SL, Péan, C, Berger, S, Caud, N, Chen, Y, Goldfarb, L, Gomis, MI, Huang, M, Leitzell, K, Lonnoy, E, Matthews, JBR, Maycock, TK, Waterfield, T, Yelekçi, O, Yu, R, Zhou, B eds.]. Cambridge, UK/New York, NY: Cambridge University Press.
- Itkin, P, Webster, M, Hendricks, S, Oggier, M, Jaggi, M, Ricker, R, Arndt, S, Divine, DV, von Albedyll, L, Raphael, I, Rohde, J, Liston, GE.** 2021. Magnarobe snow and melt pond depth measurements from the 2019-2020 MOSAiC expedition. PAN-GAEA. DOI: <http://dx.doi.org/10.1594/PANGAEA.937781>.
- Jakel, E, Wendisch, M, Mayer, B.** 2013. Influence of spatial heterogeneity of local surface albedo on the area-averaged surface albedo retrieved from airborne irradiance measurements. *Atmospheric Measurement Techniques* **6**(3): 527–537.
- Kashiwase, H, Ohshima, KI, Nihashi, S, Eicken, H.** 2017. Evidence for ice-ocean albedo feedback in the Arctic Ocean shifting to a seasonal ice zone. *Scientific Reports* **7**: 8170. DOI: <http://dx.doi.org/10.1038/s41598-017-08467-z>.
- Kwok, R.** 2014. Declassified high-resolution visible imagery for Arctic sea ice investigations: An overview. *Remote Sensing of Environment* **142**: 44–56. DOI: <http://dx.doi.org/10.1016/j.rse.2013.11.015>.
- Langleben, M.** 1968. Albedo measurements of an Arctic ice cover from high towers. *Journal of Glaciology* **7**(50): 289–297.
- Langleben, M.** 1971. Albedo of melting sea ice in the Southern Beaufort Sea. *Journal of Glaciology* **10**(58): 101–104. DOI: <http://dx.doi.org/10.3189/S0022143000013022>.
- Langleben, MP.** 1969. Albedo and degree of puddling of a melting cover of sea ice. *Journal of Glaciology* **8**(54): 407–412.
- Lei, R, Cheng, B, Hoppmann, M, Zhang, F, Zuo, G, Hutchings, JK, Lin, L, Lan, M, Wang, H, Regnery, J, Krumpen, T, Haapala, J, Rabe, B, Perovich, DK, Nicolaus, M.** 2022. Seasonality and timing of sea ice mass balance and heat fluxes in the Arctic transpolar drift during 2019–2020. *Elementa: Science of the Anthropocene* **10**(1): 000089. DOI: <http://dx.doi.org/10.1525/elementa.2021.000089>.
- Light, B, Smith, MM, Perovich, DK, Webster, MA, Holland, MM, Linhardt, F, Raphael, IA, Clemens-Sewall, D, Macfarlane, AR, Anhaus, P, Bailey, DA.** 2022. Arctic sea ice albedo: Spectral composition, spatial heterogeneity, and temporal evolution observed during the MOSAiC drift. *Elementa: Science of the Anthropocene* **10**(1): 000103. DOI: <http://dx.doi.org/10.1525/elementa.2021.000103>.
- Linhardt, F, Fuchs, N, König, M, Webster, M, von Albedyll, L, Birnbaum, G, Oppelt, N.** 2021. Comparison of complementary methods of melt pond depth retrieval on different spatial scales. EGU General Assembly 2021, online, 19–30 Apr 2021, EGU21-12860. DOI: <http://dx.doi.org/10.5194/egusphere-egu21-12860>.
- Lu, P, Cheng, B, Leppäranta, M, Li, Z.** 2018. Partitioning of solar radiation in Arctic sea ice during melt season. *Oceanologia* **60**(4): 464–477.
- Lu, P, Leppäranta, M, Cheng, B, Li, Z.** 2016. Influence of melt-pond depth and ice thickness on Arctic sea-ice albedo and light transmittance. *Cold Regions Science and Technology* **124**: 1–10.
- MacGregor, JA, Boisvert, LN, Medley, B, Petty, AA, Harbeck, JP, Bell, RE, Blair, JP, Blanchard-Wrigglesworth, E, Buckley, EM, Christoffersen, MS, Cochran, JR, Csathó, BM, De Marco, EL, Dominguez, RT, Fahnestock, MA, Farrell, SL, Gogineni, SP, Greenbaum, JS, Hansen, CM, Hofton, MA, Holt, JW, Jezek, KC, Koenig, LS, Kurtz, NT, Kwok, R, Larsen, CF, Leuschen, CJ, Locke, CT, Manizade, SS, Martin, S, Neumann, TA, Nowicki, SMJ, Paden, JD, Richter-Menge, JA, Rignot, EJ, Rodríguez-Morales, F, Siegfried, MR, Smith, BE, Sonntag, JG, Stuedinger, M, Tinto, KJ, Truffer, M, Wagner, TP, Woods, JE, Young, DA, Yungel, JK.** 2021. The Scientific Legacy of NASA's Operation IceBridge. *Reviews of Geophysics* **59**(2): e2020RG000712. DOI: <http://dx.doi.org/10.1029/2020RG000712>.
- Maslanik, J, Stroeve, J, Fowler, C, Emery, W.** 2011. Distribution and trends in Arctic sea ice age through spring 2011. *Geophysical Research Letters* **38**(13). DOI: <http://dx.doi.org/10.1029/2011GL047735>.
- Meier, W, Scambos, T, Serreze, M, Julianne, S.** 2022. Arctic Sea Ice News & Analysis (ASINA) is produced by the National Snow and Ice Data Center (NSIDC), which is part of the Cooperative Institute for Research in Environmental Sciences (CIRES) at the University of Colorado Boulder. Available at <http://nsidc.org/arcticseaicenews/>. Accessed June 6, 2023.

- Meredith, M, Sommerkorn, M, Cassotta, S, Derksen, C, Ekaykin, A, Hollowed, A, Kofinas, G, Mackintosh, A, Melbourne-Thomas, J, Muelbert, MMC, Ottersen, G, Pritchard, H, Schuur, EAG.** 2019. Chapter 3: Polar regions, in Pörtner H-O, Roberts, DC, Masson-Delmotte, V, Zhai, P, Tignor, M, Poloczanska, E, Mintenbeck, K, Alegría, A, Nicolai, M, Okem, A, Petzold, J, Rama, B, Weyer, NM eds., *IPCC special report on the ocean and cryosphere in a changing climate*. Cambridge, UK/New York, NY: Cambridge University Press: 203–320. DOI: <https://doi.org/10.1017/9781009157964.005>.
- Nicolaus, M, Perovich, DK, Spreen, G, Granskog, MA, von Albedyll, L, Angelopoulos, M, Anhaus, P, Arndt, S, Belter, HJ, Bessonov, V, Birnbaum, G, Brauchle, J, Calmer, R, Cardellach, E, Cheng, B, Clemens-Sewall, D, Dadic, R, Damm, E, de Boer, G, Demir, O, Dethloff, K, Divine, DV, Fong, AA, Fons, S, Frey, MM, Fuchs, N, Gabarró, C, Gerland, S, Goessling, HF, Gradinger, R, Haapala, J, Haas, C, Hamilton, J, Hannula, H-R, Hendricks, S, Herber, A, Heuzé, C, Hoppmann, M, Høyland, KV, Huntemann, M, Hutchings, JK, Hwang, B, Itkin, P, Jacobi, H-W, Jaggi, M, Jutila, A, Kaleschke, L, Katlein, C, Kolabutin, N, Krampe, D, Kristensen, SS, Krumpen, T, Kurtz, N, Lampert, A, Lange, BA, Lei, R, Light, B, Linhardt, F, Liston, GE, Loose, B, Macfarlane, AR, Mahmud, M, Matero, IO, Maus, S, Morgenstern, A, Naderpour, R, Nandan, V, Niubom, A, Oggier, M, Oppelt, N, Pätzold, F, Perron, C, Petrovsky, T, Pirazzini, R, Polashenski, C, Rabe, B, Raphael, IA, Regnery, J, Rex, M, Ricker, R, Riemann-Campe, K, Rinke, A, Rohde, J, Salganik, E, Scharien, RK, Schiller, M, Schneebeli, M, Semmling, M, Shimanchuk, E, Shupe, MD, Smith, MM, Smolyanitsky, V, Sokolov, V, Stanton, T, Stroeve, J, Thielke, L, Timofeeva, A, Tonboe, RT, Tavri, A, Tsamados, M, Wagner, DN, Watkins, D, Webster, M, Wendisch, M.** 2022. Overview of the MOSAiC expedition: Snow and sea ice. *Elementa: Science of the Anthropocene* **10**(1). DOI: <http://dx.doi.org/10.1525/elementa.2021.000046>.
- Niehaus, H, Spreen, G, Birnbaum, G, Istomina, L, Jäkel, E, Linhardt, F, Neckel, N, Fuchs, N, Nicolaus, M, Sperzel, T, Tao, R, Webster, M, Wright, N.** 2023. Sea ice melt pond fraction derived from Sentinel 2 data: Along the MOSAiC drift and Arctic wide. *Geophysical Research Letters* **50**(5): e2022GL102102.
- Perovich, DK.** 2005. On the aggregate-scale partitioning of solar radiation in Arctic sea ice during the Surface Heat Budget of the Arctic Ocean (SHEBA) field experiment. *Journal of Geophysical Research: Oceans* **110**(C3). DOI: <http://dx.doi.org/10.1029/2004JC002512>.
- Perovich, DK, Grenfell, TC, Light, B, Hobbs, PV.** 2002a. Seasonal evolution of the albedo of multiyear Arctic sea ice. *Journal of Geo-Physical Research: Oceans* **107**(C10): SHE 20-1–SHE 20-13. DOI: <http://dx.doi.org/10.1029/2000JC000438>.
- Perovich, DK, Grenfell, TC, Richter-Menge, JA, Light, B, Tucker, WB III, Eicken, H.** 2003. Thin and thinner: Sea ice mass balance measurements during SHEBA. *Journal of Geophysical Research: Oceans* **108**(C3). DOI: <http://dx.doi.org/10.1029/2001JC001079>.
- Perovich, DK, Light, B, Dickinson, S.** 2020. Changing ice and changing light: Trends in solar heat input to the upper Arctic Ocean from 1988 to 2014. *Annals of Glaciology* **61**(83): 401–407. DOI: <http://dx.doi.org/10.1017/aog.2020.62>.
- Perovich, DK, Tucker, WB III, Ligett, KA.** 2002b. Aerial observations of the evolution of ice surface conditions during summer. *Journal of Geophysical Research: Oceans* **107**(C10): SHE 24-1–SHE 24-14. DOI: <http://dx.doi.org/10.1029/2000JC000449>.
- Pohl, C, Istomina, L, Tietsche, S, Jäkel, E, Stapf, J, Spreen, G, Heygster, G.** 2020. Broadband albedo of Arctic sea ice from MERIS optical data. *The Cryosphere* **14**(1): 165–182. DOI: <http://dx.doi.org/10.5194/tc-14-165-2020>.
- Polashenski, C, Perovich, D, Courville, Z.** 2012. The mechanisms of sea ice melt pond formation and evolution. *Journal of Geophysical Research* **117**: C01001. DOI: <https://doi.org/10.1029/2011JC007231>.
- Rabe, B, Heuzé, C, Regnery, J, Aksenov, Y, Allerholt, J, Athanase, M, Bai, Y, Basque, C, Bauch, D, Baumann, TM, Chen, D, Cole, ST, Craw, L, Davies, A, Damm, E, Dethloff, K, Divine, DV, Doglioni, F, Ebert, F, Fang, Y-C, Fer, I, Fong, AA, Gradinger, R, Granskog, MA, Graupner, R, Haas, C, He, H, He, Y, Hoppmann, M, Janout, M, Kadko, D, Kanzow, T, Karam, S, Kawaguchi, Y, Koenig, Z, Kong, B, Krishfield, RA, Krumpen, T, Kuhlmeier, D, Kuznetsov, I, Lan, M, Laukert, G, Lei, R, Li, T, Torres-Valdés, S, Lin, L, Lin, L, Liu, H, Liu, N, Loose, B, Ma, X, McKay, R, Mallet, M, Mallett, RDC, Maslowski, W, Mertens, C, Mohrholz, V, Muilwijk, M, Nicolaus, M, O'Brien, JK, Perovich, D, Ren, J, Rex, M, Ribeiro, N, Rinke, A, Schaffer, J, Schuffenhauer, I, Schulz, K, Shupe, MD, Shaw, W, Sokolov, V, Sommerfeld, A, Spreen, G, Stanton, T, Stephens, M, Su, J, Sukhikh, N, Sundfjord, A, Thomisch, K, Tippenhauer, S, Toole, JM, Vredenburg, M, Walter, M, Wang, H, Wang, L, Wang, Y, Wendisch, M, Zhao, J, Zhou, M, Zhu, J.** 2022. Overview of the MOSAiC expedition: Physical oceanography. *Elementa: Science of the Anthropocene* **10**(1): 00062.
- Roberts, G, Ramana, M, Corrigan, C, Kim, D, Ramathan, V.** 2008. Simultaneous observations of aerosol–cloud–albedo interactions with three stacked unmanned aerial vehicles. *Proceedings of the National Academy of Sciences* **105**(21): 7370–7375.
- Rothrock, DA, Yu, Y, Maykut, GA.** 1999. Thinning of the Arctic sea-ice cover. *Geophysical Research Letters* **26**(23): 3469–3472. DOI: <http://dx.doi.org/10.1029/1999GL010863>.
- Sailor, DJ, Resh, K, Segura, D.** 2006. Field measurement of albedo for limited extent test surfaces. *Solar Energy* **80**(5): 589–599.
- Screen, JA, Simmonds, I.** 2010. The central role of diminishing sea ice in recent Arctic temperature

- amplification. *Nature* **464**(7293): 1334–1337. DOI: <http://dx.doi.org/10.1038/nature09051>.
- Serreze, MC, Holland, MM, Stroeve, J.** 2007. Perspectives on the Arctic's shrinking sea-ice cover. *Science* **315**(5818): 1533–1536. DOI: <http://dx.doi.org/10.1126/science.1139426>.
- Shupe, MD, Rex, M, Blomquist, B, Persson, POG, Schmale, J, Uttal, T, Althausen, D, Angot, H, Archer, S, Bariteau, L, Beck, I, Bilberry, J, Bucci, S, Buck, C, Boyer, M, Brasseur, Z, Brooks, IM, Calmer, R, Cassano, J, Castro, V, Chu, D, Costa, D, Cox, CJ, Creamean, J, Crewell, S, Dahlke, S, Damm, E, de Boer, G, Deckelmann, H, Dethloff, K, Dütsch, M, Ebell, K, Ehrlich, A, Ellis, J, Engelmann, R, Fong, AA, Frey, MM, Gallagher, MR, Ganzeveld, L, Gradinger, R, Graeser, J, Greenamyre, V, Griesche, H, Griffiths, S, Hamilton, J, Heinemann, G, Helmig, D, Herber, H, Heuzé, C, Hofer, J, Houchens, T, Howard, D, Inoue, J, Jacobi, H-W, Jaiser, R, Jokinen, T, Jourdan, O, Jozef, G, King, W, Kirchgaessner, A, Klingebiel, M, Krassovski, M, Krumpfen, T, Lampert, A, Landing, W, Laurila, T, Lawrence, D, Lonardi, M, Loose, B, Lüpkes, C, Maahn, M, Macke, A, Maslowski, W, Marsay, C, Maturilli, M, Mech, M, Morris, S, Moser, M, Nicolaus, M, Ortega, P, Osborn, J, Pätzold, F, Perovich, DK, Petäjä, T, Pilz, C, Pirazzini, R, Posman, K, Powers, H, Pratt, KA, Preußner, A, Quéléver, L, Radenz, M, Rabe, B, Rinke, A, Sachs, T, Schulz, A, Siebert, H, Silva, T, Solomon, A, Sommerfeld, A, Spreen, G, Stephens, M, Stohl, A, Svensson, G, Uin, J, Viegas, J, Voigt, C, von der Gathen, P, Wehner, B, Welker, JM, Wendisch, M, Werner, M, Xie, Z, Yue, F.** 2022. Overview of the MOSAiC expedition: Atmosphere. *Elementa: Science of the Anthropocene* **10**(1). DOI: <http://dx.doi.org/10.1525/elementa.2021.00060>.
- Siegel, R, Howell, J.** 1981. *Thermal radiation heat transfer*. Washington, DC: Hemisphere.
- Smith, MM, Light, B, Macfarlane, AR, Perovich, DK, Holland, MM, Shupe, MD.** 2022. Sensitivity of the Arctic sea ice cover to the summer surface scattering layer. *Geophysical Research Letters* **49**(9): e2022GL098349. DOI: <http://dx.doi.org/10.1029/2022GL098349>.
- Stapf, J, Ehrlich, A, Jäkel, E, Lüpkes, C, Wendisch, M.** 2020. Reassessment of shortwave surface cloud radiative forcing in the Arctic: Consideration of surface-albedo–cloud interactions. *Atmospheric Chemistry and Physics* **20**(16): 9895–9914. DOI: <http://dx.doi.org/10.5194/acp-20-9895-2020>.
- Stroeve, JC, Markus, T, Boisvert, L, Miller, J, Barrett, A.** 2014. Changes in Arctic melt season and implications for sea ice loss. *Geophysical Research Letters* **41**: 1216–1225. DOI: <http://dx.doi.org/10.1002/2013GL058951>.
- Thackeray, CW, Hall, A.** 2019. An emergent constraint on future Arctic sea-ice albedo feedback. *Nature Climate Change* **9**(12): 972–978.
- Tschudi, MA, Maslanik, JA, Perovich, DK.** 2008. Derivation of melt pond coverage on Arctic sea ice using MODIS observations. *Remote Sensing of Environment* **112**(5): 2605–2614. DOI: <http://dx.doi.org/10.1016/j.rse.2007.12.009>.
- Uttal, T, Curry, JA, McPhee, MG, Perovich, DK, Moritz, RE, Maslanik, JA, Guest, PS, Stern, HL, Moore, JA, Turenne, R, Heiberg, A.** 2002. Surface heat budget of the Arctic Ocean. *Bulletin of the American Meteorological Society* **83**(2): 255–276. DOI: [http://dx.doi.org/10.1175/1520-0477\(2002\)083<0255:SHBOTA>2.3.CO;2](http://dx.doi.org/10.1175/1520-0477(2002)083<0255:SHBOTA>2.3.CO;2).
- Vihma, T.** 2014. Effects of Arctic sea ice decline on weather and climate: A review. *Surveys in Geophysics* **35**(5): 1175–1214. DOI: <http://dx.doi.org/10.1007/s10712-014-9284-0>.
- Wang, M, Su, J, Li, T.** 2018. Determination of Arctic melt pond fraction and sea ice roughness from Unmanned Aerial Vehicle (UAV) imagery. *Advances in Polar Science* **29**: 181–189.
- Warren, SG.** 1982. Optical properties of snow. *Reviews of Geophysics* **20**(1): 67–89. DOI: <http://dx.doi.org/10.1029/RG020i001p00067>.
- Webster, MA, Holland, M, Wright, NC, Hendricks, S, Hutter, N, Itkin, P, Light, B, Linhardt, F, Perovich, DK, Raphael, IA, Smith, MM, von Albedyll, L, Zhang, J.** 2022. Spatiotemporal evolution of melt ponds on Arctic sea ice: MOSAiC observations and model results. *Elementa: Science of the Anthropocene* **10**(1): 000072.
- Webster, MA, Rigor, IG, Perovich, DK, Richter-Menge, JA, Polashenski, CM, Light, B.** 2015. Seasonal evolution of melt ponds on Arctic sea ice. *Journal of Geophysical Research: Oceans* **120**(9): 5968–5982. DOI: <http://dx.doi.org/10.1002/2015JC011030>.
- Wright, NC, Polashenski, CM.** 2018. Open-source algorithm for detecting sea ice surface features in high-resolution optical imagery. *The Cryosphere* **12**: 1307–1329. DOI: <https://doi.org/10.5194/tc-12-1307-2018>.
- Wright, NC, Polashenski, CM, McMichael, ST, Beyer, RA.** 2020. Observations of sea ice melt from Operation IceBridge imagery. *The Cryosphere* **14**(10): 3523–3536. DOI: <http://dx.doi.org/10.5194/tc-14-3523-2020>.
- Wright, NC, Webster, M, Polashenski, C.** 2021. Melt Pond Maps around the Multi-disciplinary drifting Observatory for the Study of Arctic Climate (MOSAiC) Drifting Station derived from High Resolution Optical Imagery, 2020. Arctic Data Center. DOI: <http://dx.doi.org/10.18739/A2833N04M>.
- Wunderling, N, Willeit, M, Donges, JF, Winkelmann, R.** 2020. Global warming due to loss of large ice masses and Arctic summer sea ice. *Nature Communications* **11**: 5177. DOI: <http://dx.doi.org/10.1038/s41467-020-18934-3>.
- Zhu, J, Liu, Y, Wang, X, Li, T.** 2021. Optical properties and surface energy flux of spring fast ice in the Arctic. *Acta Oceanologica Sinica* **40**: 84–96.

How to cite this article: Calmer, R, de Boer, G, Hamilton, J, Lawrence, D, Webster, MA, Wright, N, Shupe, MD, Cox, CJ, Cassano, JJ. 2023. Relationships between summertime surface albedo and melt pond fraction in the central Arctic Ocean: The aggregate scale albedo obtained on the MOSAiC floe. *Elementa: Science of the Anthropocene* 11(1). DOI: <https://doi.org/10.1525/elementa.2023.00001>

Domain Editor-in-Chief: Detlev Helmig, Boulder AIR LLC, Boulder, CO, USA

Guest Editor: MingXi Yang, Plymouth Marine Laboratory, Plymouth, UK

Knowledge Domain: Atmospheric Science

Part of an Elementa Special Feature: The Multidisciplinary Drifting Observatory for the Study of Arctic Climate (MOSAiC)

Published: June 15, 2023 **Accepted:** April 22, 2023 **Submitted:** December 22, 2022

Copyright: © 2023 The Author(s). This is an open-access article distributed under the terms of the Creative Commons Attribution 4.0 International License (CC-BY 4.0), which permits unrestricted use, distribution, and reproduction in any medium, provided the original author and source are credited. See <http://creativecommons.org/licenses/by/4.0/>.



Elem Sci Anth is a peer-reviewed open access journal published by University of California Press.

OPEN ACCESS 